Impact of the noise knowledge uncertainty for the science exploitation of cosmological and astrophysical stochastic gravitational wave background with LISA

Martina Muratore,[1,*] Jonathan Gair,[1] and Lorenzo Speri[1]

[1] *Max Planck Institute for Gravitational Physics (Albert Einstein Institute), D-14476 Potsdam, Germany*

(Dated: August 3, 2023)

This paper investigates the impact of a lack of knowledge of the instrumental noise on the characterisation of stochastic gravitational wave backgrounds with the Laser Interferometer Space Antenna (LISA). We focus on constraints on modelled backgrounds that represent the possible backgrounds from the mergers of binary black holes of stellar origin, from primordial black hole generation, from non-standard inflation, and from sound wave production during cosmic fluid phase transitions. We use splines to model generic, slowly varying, uncertainties in the auto and cross-spectral densities of the LISA time delay interferometry channels. We find that allowing for noise knowledge uncertainty in this way leads to one to two orders of magnitude degradation in our ability to constrain stochastic backgrounds, and a corresponding increase in the background energy density required for a confident detection. We also find that to avoid this degradation, the LISA noise would have to be known at the sub-percent level, which is unlikely to be achievable in practice.

I. INTRODUCTION

The Laser Interferometer Space Antenna (LISA) is part of the European Space Agency Cosmic Vision program and is due to be launched in the mid-2030s. LISA will be the first observatory in space to study gravitational waves (GWs) at mHz frequencies. It will consist of a constellation of three satellites forming a quasi equilateral triangle and continuously exchanging laser beams [4]. LISA is expected to observe a large variety of sources, such as galactic binaries (GBs), massive black hole binaries (MBHBs) [29], stellar-origin black hole binaries (SOBHB) [22, 31, 43], extreme-mass-ratio inspirals (EMRIs) [8] and possibly stochastic backgrounds arising from astrophysical and cosmological processes [16].

When considering the science that can be done with LISA, it is typical to assume a known model for the instrumental noise in the detector data channels. However, these noise levels will not be known in practice. This is also true for ground-based gravitational wave detectors, but in that context spectral density estimation is easier because signals are rare and short-lived, allowing the spectral density to be estimated from data in the vicinity of observed events. LISA signals, by contrast, are typically long lived, which means that noise and signal properties must be simultaneously estimated by fitting a suitable model. While such methods and models are still under development, it is expected that the characterisation of deterministic signals will not be significantly affected by lack of instrumental noise knowledge (see Appendix B 4). The case of stochastic GW backgrounds (SGWB) is different, however, as these are intrinsically of the same character as the stochastic instrumental noise. Searches for stochastic signals in ground-based interferometers rely on the cross-correlation of data from independent detectors [3]. This would only be possible if there is another space-based interferometer in operation concurrently, such as Taiji [40], but this is not certain at the moment. Here we explore the challenge of distinguishing between the stochastic instrumental noise and a stochastic GW signal.

One approach is to use a model for the instrumental noise. It is possible to derive analytical models that describe how different known noise sources propagate into the LISA data stream. However, not all noise sources will be known in advance, so we will not be able to strictly rely on the models as we will not be able to perform full tests and directly measure the noise. In the LISAPathfinder mission [5] it was seen that at low frequency the analytical models couldn't fully explain the measured noise. Therefore, when we plan for LISA data analysis, we must be prepared for uncertainty in the noise models.

The goal of this paper is to assess the impact of lacking a noise model for LISA in parameter estimation of SGWBs. We consider four different models of cosmological and astrophysical SGWBs: a power law to model signals from stellar origin binary black hole inspirals, a Gaussian bump to model a background from primordial black hole generation, a power law with running to model a background from non-standard inflation and finally a first order phase transition model, representing GW production from sound waves in the cosmic fluid generated by colliding phase transition bubbles [16]. For each model, we will take a reference amplitude that corresponds to a relatively low signal to noise ratio (SNR) that is close to the boundary for detection. These are the backgrounds that will be most difficult to distinguish from instrumental noise. We will also explore what happens as the background energy density is varied in each model.

We represent our lack of knowledge of the LISA instrumental noise by multiplying a set of reference auto- and cross-spectral densities with cubic splines. For

* contact: martina.muratore@aei.mpg.de

the reference spectral densities we use the noise model from [4], which includes only the so-called secondary noises [33], the test mass (TM) acceleration and optical metrology noise (OMS). This noise model assumes that the laser noise [6], clock noise [46], tilt to length coupling [23, 37] have been suppressed by the initial noise reduction pipeline [24, 32]. To represent the fact that we will have some amount of information from noise modelling before launch, we place a Gaussian prior on the weights of the cubic spline. By varying the Gaussian variance we explore the effect of having more or less knowledge of the noise.

Several previous studies have tackled the problem of detecting a SGWB with LISA and distinguishing it from the noise, but these have used different methods than the one we employ in this paper. In [20] it was shown that SGWB reconstruction was possible for generic SGWB models, if the LISA instrumental noise can be represented by just two parameters, representing the level of TM and OMS noise, assumed equal for all arms of the interferometer. The authors of [2, 26] allowed the TM and OMS noises to differ from arm to arm, but still assumed that these noises had a known spectral shape as a function of frequency. In [10] an arbitrary noise shape was allowed, described by a spline, but using a simplified noise model for the single link. Finally, [33] derived an upper bound on the detectable SGWB amplitude when being agnostic on both the signal and noise shape and discussed limitations of the utility of the null channel for distinguishing between instrumental noise and a stochastic GW background.

The paper is organised as follows: in Section II we introduce the general data model that we use in the analysis and we describe the Fisher matrix formalism that will be used for this work. In Section II C we describe the spline model that we use to represent the uncertainties in the power spectral density (PSD) and cross-spectral density (CSD) of the instrumental noise. In Section II D we give the analytical noise model for a single LISA link that is used as the reference model, and the corresponding PSDs and CSDs for the time delay interferometry (TDI) channels, A, E and ζ. In Section II E we describe how a stochastic signal appears in the three TDI channels and their cross-correlations, while in Section II F we describe the models for the cosmological and astrophysical SGWBs that we use in this paper. In Section III A we show how well we can estimate the parameters of the different SGWB models when we allow for uncertainty in our knowledge of the instrumental noise. For each model, we compare the precision of parameter estimation to that when noise knowledge is perfect and show how the parameter precisions vary as a function of the background energy density, Ω, evaluated at 1mHz. In Section III B we show how the results change as we vary our priors uncertainty on the instrumental noise. We conclude our results in Section III C by showing how well the signal, noise and galactic foreground can be reconstructed for a power law SGWB background. Section IV summarises our conclusions and future perspectives.

II. METHODS

A. Likelihood

We assume that the output of a gravitational wave detector, $s(t)$, is expressed as a linear combination of a signal, $h(t|\vec{\mu})$, determined by a finite set of (unknown) parameters, $\vec{\mu}$, and instrumental noise, $n(t)$. If we ignore the presence of calibration errors [42], the content of a single data stream, i.e., one output channel from one detector, can be written in the frequency domain as:

$$\tilde{s}(f) = \tilde{h}(f|\vec{\mu}) + \tilde{n}(f), \tag{1}$$

where the tilde indicates the Fourier transform. The likelihood for the observed data can be written as $p(\tilde{s}(f)|\vec{\mu}) = p(\tilde{n}(f) = \tilde{s}(f) - \tilde{h}(f|\vec{\mu}))$. In a gravitational wave context it is usual to further assume that the instrumental noise follows a Gaussian distribution characterized by a one-sided PSD, $S_n(f)$, defined such that

$$\mathbb{E}[\tilde{n}^*(f)\tilde{n}(f')] = \frac{1}{2}S_n(f)\delta(f - f'), \tag{2}$$

for f, $f' > 0$, where the expectation value $\mathbb{E}$ is taken over the data generating process. The delta function in the previous equation implies that different frequencies are not correlated.

In reality the noise model is not known perfectly and could vary from the assumption above in a number of ways. For example, the PSD might have a different shape from the reference one [9], the probability distribution of the noise might not be Gaussian, or the noise might not be stationary, leading to correlations between frequencies.

In this work we will continue to assume that the noise is Gaussian and stationary, but we will allow the power spectral density to vary using a parametrized spectral density, $S_n(f) \to S_n(f|\vec{\lambda})$, described by parameters $\vec{\lambda}$. Then the log-likelihood depends on both sets of parameters, $\vec{\mu}$ and $\vec{\lambda}$, and can be written as:

$$l := \ln p(\tilde{s}|\vec{\mu}, \vec{\lambda}) = -\sum_{k=1}^{n} \ln\left[2\pi \frac{S_n(f_k|\vec{\lambda})}{4\Delta f}\right] - \tag{3}$$

$$\frac{1}{2}\sum_{k=1}^{n} \frac{|\tilde{s}(f_k) - \tilde{h}(f_k|\vec{\mu})|^2}{\frac{1}{4\Delta f}S_n(f_k|\vec{\lambda})} \tag{4}$$

where the sum is performed over n frequencies and $\tilde{n}(f_k) = \tilde{s}(f_k) - \tilde{h}(f_k|\vec{\mu})$ are the discrete Fourier component at frequency $f_k = k\Delta f$, of the data minus signal model. The frequency bin width, Δf, is related to the total observation time as $T = 1/\Delta f$. The first term does

not include the 1/2 factor because the real and imaginary parts of $\tilde{n}(f_k)$ are independent random variables. This follows from the fact that, for a real time series, $\tilde{n}^*(f) = \tilde{n}(-f)$, which combined with Eq. (2) means that $\langle \tilde{n}(f)\tilde{n}(f')\rangle = 0$ for $f,\ f' > 0$. This allows equation 2 to be rewritten as

$$\langle \Re[\tilde{n}(f_k)]^2\rangle = \langle \Im[\tilde{n}(f_k)]^2\rangle = \frac{\langle |\tilde{n}(f_k)|^2\rangle}{2} = \frac{S_n(f_k|\vec{\lambda})}{4\Delta f} \quad (5)$$

for a discrete set of frequencies.

Stochastic gravitational wave backgrounds are not deterministic signals and can be treated on the same footing as the instrumental noise by defining the total variance at frequency f_k as

$$S_t(f_k|\vec{\theta},\vec{\lambda}) = S_{\rm GW}(f_k|\vec{\theta}) + S_{\rm n}(f_k|\vec{\lambda})\,. \quad (6)$$

If we assume that all the deterministic sources have been correctly subtracted from the datastream s the log-likelihood becomes:

$$l(\vec{\theta},\vec{\lambda}) = -\sum_{k=1}^{n} \ln\left[T\pi\frac{S_t(f_k|\vec{\theta},\vec{\lambda})}{2}\right] - \frac{1}{2}\sum_{k=1}^{n}\frac{|\tilde{s}(f_k)|^2}{\frac{T}{4}S_t(f_k|\vec{\theta},\vec{\lambda})} \quad (7)$$

The derivation of this likelihood can be found in Appendix A.

B. Fisher matrix

We are interested in understanding the impact of noise knowledge uncertainties on the parameter measurement precision of stochastic gravitational wave backgrounds. The Fisher information matrix provides a lower bound on the covariance of an unbiased estimator of the model parameters and provides a good approximation to the precision of parameter estimation in the high signal-to-noise ratio limit. We will therefore use it to quantify our ability to measure both the noise parameters, $\vec{\lambda}$, and the background parameters, $\vec{\theta}$.

In a general context the Fisher matrix is defined by

$$\Gamma_{ij} = \mathbb{E}\left[\frac{\partial l}{\partial v^i}\frac{\partial l}{\partial v^j}\right] = -\mathbb{E}\left[\frac{\partial^2 l}{\partial v^i \partial v^j}\right] \quad (8)$$

where the expectation value $\mathbb{E}$ is taken over the data generating process, and the partial derivatives are taken with respect to the parameters, $\vec{v}$, on which the likelihood depends. We want to compute the Fisher matrix on the extended parameter space $\vec{v} = \{\vec{\theta},\vec{\lambda}\}$.

It can be shown that the expectation value of the product between the derivative of the log-likelihood with respect to deterministic and stochastic parameters is zero. Therefore, at the level of the Fisher matrix approximation it can be shown that the estimation of the noise and deterministic signal parameters is independent (see Appendix B 4).

For SGWBs, we can compute the Fisher matrix in continuous domain as:

$$\Gamma_{ij} = T\int_0^\infty (\Sigma^{-1})_{lr}\frac{\partial \Sigma^{rp}}{\partial v^i}(\Sigma^{-1})_{pm}\frac{\partial \Sigma^{ml}}{\partial v^j}\,{\rm d}f\,. \quad (9)$$

with

$$\Sigma(f|\vec{v} = \{\vec{\theta},\vec{\lambda}\}) = \frac{1}{2}\begin{pmatrix} S_t^{AA} & S_t^{AE} & S_t^{A\zeta} \\ S_t^{AE*} & S_t^{EE} & S_t^{E\zeta} \\ S_t^{A\zeta*} & S_t^{E\zeta*} & S_t^{\zeta\zeta}\end{pmatrix}\,. \quad (10)$$

where each element of the matrix can be written as a sum of an instrumental noise component and a stochastic gravitational wave component as indicated in Eq. 6. A complete derivation of this formula can be found in Appendix B.

Prior knowledge on the noise can be incorporated by imposing a prior on the instrumental parameters, $\vec{\lambda}$. When doing numerical marginalisation any prior can be imposed, but in the Fisher matrix formalism it is easiest to work with a Gaussian prior [42]. The posterior covariance is then given by the inverse of the modified Fisher matrix:

$$\Gamma = \begin{pmatrix} \Gamma^{\theta\theta} & \Gamma^{\theta\lambda} \\ (\Gamma^{\theta\lambda})^T & \Gamma^{\lambda\lambda} + \Theta^{\lambda\lambda}\end{pmatrix} \quad (11)$$

with normal prior on the instrumental noise parameters with zero mean and covariance given by $(\Theta^{\lambda\lambda})^{-1}$. The diagonal elements of the inverse of this matrix provide estimates for the precision with which the corresponding parameters can be measured. The estimated precision of measurement of the SGWB parameters accounting for noise model uncertainty is thus given by the diagonal elements of the matrix:

$$\sigma_\theta = \sqrt{{\rm diag}[(\Gamma^{\theta\theta} - \Gamma^{\theta\lambda}(\Gamma^{\lambda\lambda} + \Theta^{\lambda\lambda})^{-1}(\Gamma^{\theta\lambda})^T)^{-1}]} \quad (12)$$

Note that in the limit in which the instrumental noise parameters are perfectly known $\Theta \to \infty$ and the measurement precision of the SGWB parameters is given by $\sigma_\theta = \sqrt{{\rm diag}[(\Gamma^{\theta\theta})^{-1}]}$.

C. Modeling noise knowledge uncertainties

To model noise uncertainties, we allow the PSD and CSD of the instrumental channels to deviate from the design specification. However, we assume that such deviations vary smoothly over a relatively wide range of frequency and model the noise uncertainties as fractional deviations from the design PSD/CSD that are described by natural cubic splines. We write the PSD of the instrumental noise in each channel as:

$$S_n(f|\lambda) = S_{\rm des}(f)\,10^{C(f|\vec{\lambda})}\,, \quad (13)$$

where $C(f|\vec{\lambda})$ is a natural cubic spline. The parameters $\vec{\lambda}$ specify the values of the spline at the knots, labelled by i. In this study we use knots evenly spaced in $\log_{10}(f)$ between $\log_{10}(f) = -4$ and $\log_{10}(f) = 0$ and we fix the number of knots to 13. Noise curves corresponding to this model, with the weights at each knot drawn randomly from a $\log_{10}(f) \sim U[-1, 1]$ distribution, are shown in fig. 1. We note that this choice of prior means we are allowing approximately one order of magnitude variation in the PSD. When we evaluate the Fisher matrix we will always do so at the reference point where the weights of the spline are zero, i.e., where the PSD is equal to the reference value shown in Fig. 2.

We cannot follow the same procedure for specifying the CSD, because the reference model is smaller by 1 or even 2-3 order of magnitude a low frequency with respect to the PSD (see Fig. 3 and Fig. 2). It was shown in [26] that when the LISA response is constructed allowing for unequal noises in the different laser links, the CSD can be much larger and become comparable to the PSD. Since our goal is to allow the splines to vary in such a way to mimic un-expected and un-modelled noise components with respect to the simplified scenario (three unequal but fixed-length arms) we model the CSD as[1]:

$$\begin{aligned} S_n(f|\{\lambda_i\}) = & \\ & \sqrt{S_{\rm des,i}(f) S_{\rm des,i}(f)}\, \sigma_R\, 10^{C(f|\{\log_{10}(f_i)\},\{\lambda_i\})} \\ & + \sqrt{S_{\rm des,i}(f) S_{\rm des,i}(f)}\, i\sigma_I\, 10^{C(f|\{\log_{10}(f_i)\},\{\lambda_i\})} \end{aligned} \tag{14}$$

where we fix $\sigma_R = 0.1, \sigma_I = 0.8\sigma_R$. We do not expect that varying the relationship between σ_I and σ_R to significantly change the conclusions; although we fix σ_I slightly smaller than σ_R accordingly to Fig. 3. There at lower frequencies the imaginary components are about 1 order of magnitude smaller than the real components. The indexes i and j run over the number of detectors or channels with $i \neq j$. The additional factors σ_I and σ_R are used to limit the amplitude, and allow us to model the CSD as a sum of splines times the geometric mean of the square root-PSDs. Using the (scaled-)geometric mean of the PSDs as a reference for the CSD rather than the CSD of the reference equal-noise configuration, allows for much larger CSD variations. This is consistent with the results presented in [26].

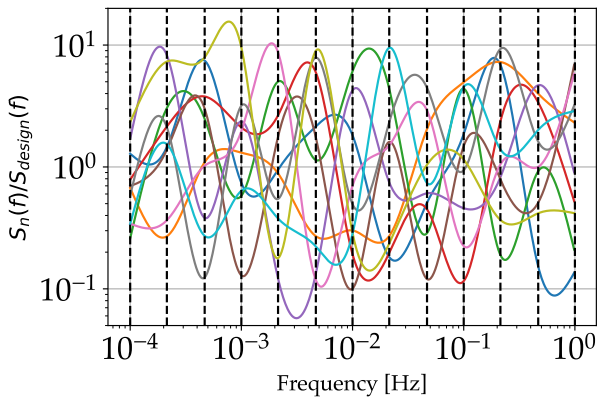

FIG. 1. Deviations from the design power spectral density obtained using the cubic spline model, with $\lambda_i \sim U[-1, 1]$, and with knots equally spaced between $\log_{10}(f) = -4$ and $\log_{10}(f) = 0$. The plot shows the ratio of the total PSD and the design one for different parameter realizations λ_i.

It is important to state that our model is not completely general since we are imposing a certain amount of smoothness in the PSD variation, and consequently in the CSD, when we specify the number and spacing of the knots. Thus we are not able to fit for all possible noise scenarios. In particular, this model does not attempt to reproduce the zeros of the TDI transfer functions faithfully. This will become important above $f \sim 0.05$Hz, but this should not affect our results as the SGWBs we consider do not have much power at those frequencies, as can be seen from Fig. 6. Other models could be considered, for example by imposing the spline variations at the level of the noise in individual laser links (generalising the approach taken in [10]), before applying the TDI transfer function. This should be explored in the future, but this would increase the number of parameters further so we might expect there to be additional degeneracies, which would lead to practical difficulties in fitting noise and signal simultaneously. However, for the purpose of the current study, the model we use is adequate to represent generic, slowly varying, fluctuations in the PSD and CSD.

[1] In principle our model does not force the matrix to be positive definite. We are forcing the reference spectral density matrix to be positive definite, but in principle we could have a factor of 10 variation in the CSD while the PSD is unchanged. It doesn't matter for the Fisher matrix because this is a local approximation and we are evaluating it at a point where the matrix is positive definite. The CSD at the central point is 0.1 of its maximum value, so in an open set around that point it will be positive definite and thus all derivatives are well defined. The conclusion is that the model used here is fair for what we want to demonstrate but would not be a suitable model to use when analysing the data.

D. Noise at the TDI input and outputs

Here, we present the instrumental noise model used to define the reference PSD in this work. Among the different noise sources for LISA, the laser noise is the main source of noise, which must be reduced by eight orders of magnitude by applying a post-processing technique called time delay interferometry (TDI) [45]. TDI synthesises an equal arm-length interferometer by

appropriately delaying and combining the interferometric measurements in many different ways to form TDI channels free from laser noise. The standard second generation TDI channels (unequal and time varying arm-length) are the Michelson interferometer channels, X, Y and Z, from which we form the more GW sensitive channels, A and E [39]. Together with the GW sensitive channels we consider a null channel, the ζ channel [35] that is less sensitive to GWs and can in principle be used as a noise monitor.

In the current work we will assume that laser noise has already been reduced thus we can work directly with the first generation TDI [27], allowing us to consider three unequal but fixed arm-lengths. This choice should not significantly affect the conclusions of the analysis but simplifies the transfer function derivations.

We also assume that all known calibrated and measured instrumental noise sources have been subtracted, such as the optical tilt to length cross-coupling to spacecraft motion and clock noise ([23], [18] and [25]). The remaining noises, for which we have neither a measurement for coherent subtraction nor a high precision a priori model [33], fall into two broad categories, the acceleration noise of each individual test-mass (TM) and an overall optical metrology system (OMS) noise term for each single link measurement (see [36] for the case of multiple OMS noise terms).

We represent the TM acceleration noise PSD of a single TM by $S_{g_{ij}}$. To directly compare the OMS and TM contributions we can directly convert the acceleration noise of a single TM to an equivalent displacement, whose PSD is given by

$$S^{\rm disp}_{g_{ij}} = S_{g_{ij}}/(2\pi f)^4 \tag{15}$$

where f is the Fourier frequency. We denote the time series associated with this displacement as $x^g_{ij}(t)$. We also define the PSD of the OMS noise as $S_{{\rm oms}_{ij}}(f)$ and we denote the time series of the single OMS as $x^m_{ij}(t)$. All TDI combinations can be constructed from a combination of single link TM to TM measurements. Such measurements are represented by the intermediary variables [24]:

$$\tilde{\eta}^N_{ij}(\omega) = \tilde{x}(\omega)^g_{ji} e^{-i\omega L_{ji}} + \tilde{x}(\omega)^g_{ij} + \tilde{x}(\omega)^m_{ij}, \tag{16}$$

where $\tilde{\eta}^N_{ij}(\omega)$ is the noise in a single link measurement, the first index i indicates the spacecraft where the measurement is performed at time t, and the second index j indicates the distant spacecraft from which light was emitted at time $t-\tau$, and $\omega = 2\pi f$. Equation 16 implies that each single link measurement contains TM noise terms from the distant and local spacecraft, such that the TM noise appearing in the measurements on the two ends of the same arm is correlated (between the two links):

$$\langle \tilde{\eta}^N_{ij}(\omega)\tilde{\eta}^N_{ji}(\omega)\rangle \neq 0 \tag{17}$$

From these measurements it is possible to build any TDI channels [6, 34] and therefore the corresponding first generation orthogonal channels A_1 and E_1 [27] that will be used in this work:

$$\mathrm{A_1} = \frac{\mathrm{Z_1} - \mathrm{X_1}}{\sqrt{2}}\,, \qquad \mathrm{E_1} = \frac{\mathrm{X_1} - 2\mathrm{Y_1} + \mathrm{Z_1}}{\sqrt{6}}. \tag{18}$$

The X_1 variable is defined as:

$$\begin{aligned}\mathrm{X_1} =& (D_{13}D_{31} - 1)(\eta_{12} + D_{12}\eta_{21}) \\ &+ (1 - D_{12}D_{21})(\eta_{13} + D_{13}\eta_{31})\,,\end{aligned} \tag{19}$$

where the delays D_{ij} corresponds to a constant time shift and thus in frequency to $\mathcal{F}\{D_{ij}\} = e^{-i\omega L_{ij}}$. The Y_1 and Z_1 are given from X_1 by cyclic permutations of the three satellites. The fully symmetric channel, ζ_1, is defined by:

$$\zeta_1 = D_{12}(\eta_{31} - \eta_{32}) + D_{23}(\eta_{12} - \eta_{13}) + D_{31}(\eta_{23} - \eta_{21})\,. \tag{20}$$

The assumed model for the TM acceleration noise is

$$\begin{aligned}&\mathrm{E}\left\langle \tilde{x}^g_{ij}(f)\tilde{x}^{g*}_{lm}(f')\right\rangle = \frac{1}{2}\delta_{il}\delta_{jm}\delta(f-f')S_{g_{ij}}(f) \\ &S_{g_{ij}}(f) = \left(3\times 10^{-15}\ \frac{\mathrm{m}}{\mathrm{s}^2\ \sqrt{\mathrm{Hz}}}\right)^2 \\ &\times\left(1+\left(\frac{0.4\ \mathrm{mHz}}{f}\right)^2\right)\left(1+\left(\frac{f}{8\ \mathrm{mHz}}\right)^4\right),\end{aligned} \tag{21}$$

and for the OMS noise

$$\begin{aligned}&\mathrm{E}\left\langle \tilde{x}^m_{ij}(f)\tilde{x}^{m*}_{lm}(f')\right\rangle = \frac{1}{2}\delta_{il}\delta_{jm}\delta(f-f')S_{{\rm oms}_{ij}}(f) \\ &S_{{\rm oms}_{ij}}(f) = \left(15\ \mathrm{pm}/\sqrt{\mathrm{Hz}}\right)^2 \times\left(1+\left(\frac{2\ \mathrm{mHz}}{f}\right)^4\right),\end{aligned} \tag{22}$$

This model assumes that individual noise components are uncorrelated. In reality the test masses in the same satellite will share environmental noise, such as temperature fluctuations, so this assumption might not hold. However, this model serves as a reference one, and any variation is captured by the flexible spline model previously presented.

To derive the PSDs and CSDs of the TDI channels A, E and ζ, as illustrated in [35], one can express the arm-lengths L_{ij} in terms of the breathing modes of the LISA triangle, δ_a and δ_b as:

$$L_{12}(t) = L\left[1 + \frac{1}{2}\left(\sqrt{3}\,\delta_a - \delta_b\right)\right]\,, \tag{23a}$$

$$L_{23}(t) = L\left(1 + \delta_b\right)\,, \tag{23b}$$

$$L_{31}(t) = L\left[1 - \frac{1}{2}\left(\sqrt{3}\,\delta_a + \delta_b\right)\right]\,. \tag{23c}$$

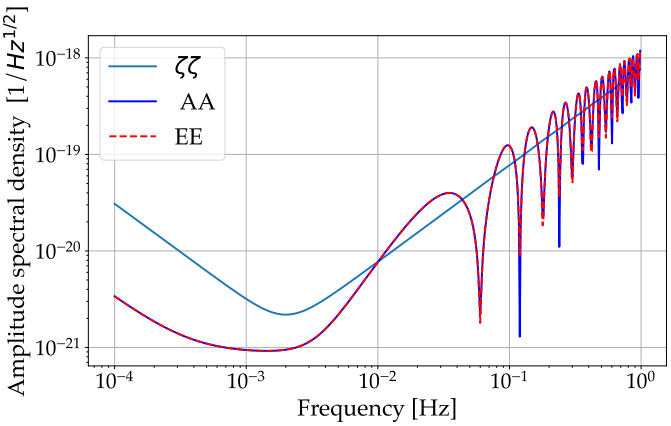

FIG. 2. Reference Amplitude spectral density for the Time delay interferometry channels A, E and ζ considering only test mass acceleration and optical metrology noise and assuming a constellation of three fixed unequal arm-lengths.

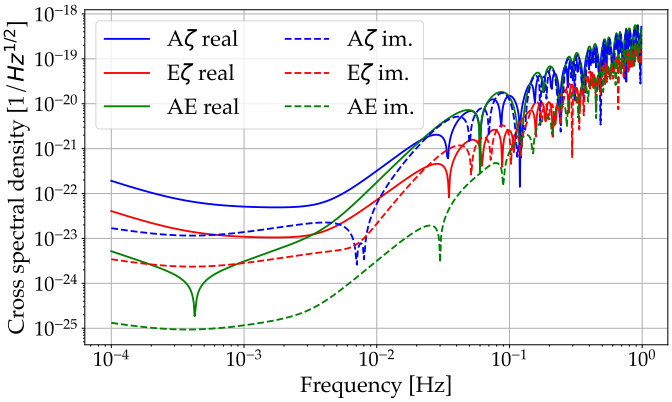

FIG. 3. Real and imaginary part of the reference square root of the cross spectral density for the time delay interferometry channels AE, Eζ and Aζ considering only TM acceleration and OMS noise and assuming a constellation of three fixed unequal arm-lengths.

The full expressions are rather long thus we give them in a separate *Mathematica* notebook file (noise-analytical-model) and we plot them in Fig. 2. The Amplitude spectral density (ASD) are computed in terms of δ_a and δ_b. Indeed, while $L = (L_{12} + L_{23} + L_{31})/3 \approx 8.3\,\mathrm{s}$ is the average arm-length, the small parameters δ_a and δ_b are typically $\sim 0.005 - 0.009$ for realistic ESA orbits [14]. The case $\delta_a = \delta_b = 0$ corresponds to the equal-arm LISA scenario.

We consider that the six TMs have the same PSD as well as the six OMS noise terms, but this suppresses the contribution in the CSD. It was shown in [26] that if the levels of the noises differ by 20% then the CSD can be 10% of the PSD at low frequencies and several tens of percent at high frequency. This motivates the particular choice of flexible CSD model that we introduced in Eq. (14) and is illustrated in Fig. 4.

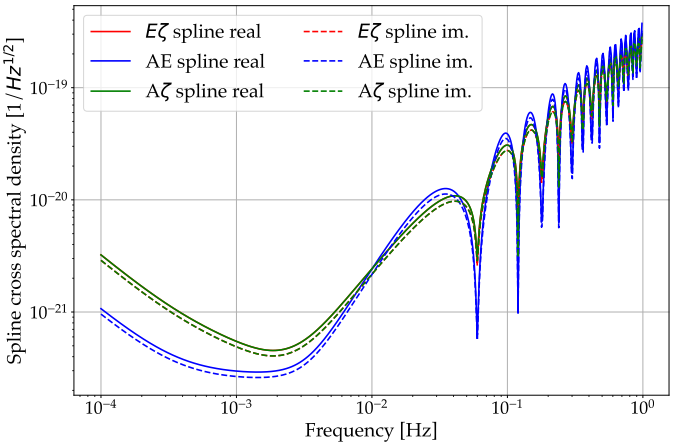

FIG. 4. Real and Imaginary part of splines-square root cross spectral density for the time delay interferometry channels AE, Eζ and Aζ considering test mass acceleration and optical metrology noise assuming a constellation of three fix unequal arm-lengths

E. Signal transfer function

The detector response to a stochastic background can be computed by expressing a GW signal as a superposition of plane waves, and by assuming that the LISA constellation has static arm lengths and is in a flat background spacetime. Following [26], it is possible to show that the component of the single link measurement $\eta_{ij}(t)$ due to a GW is given by:

$$\eta_{ij}^{GW}(t) = i \int_{-\infty}^{\infty} \left\{ \frac{f}{f_{ij}} \mathrm{e}^{2\pi i f(t-L_{ij})} \int \left[\mathrm{e}^{-2\pi i f \hat{k}\cdot\vec{x}_i} \sum_{\mathcal{A}} \xi_{ij}^{\mathcal{A}}(f,\hat{k}) \tilde{h}_{\mathcal{A}}(f,\hat{k}) \right] \mathrm{d}\Omega_{\hat{k}} \right\} \mathrm{d}f, \tag{24}$$

where i stands for imaginary component, $f_{ij} = (2\pi L_{ij})^{-1}$, $\vec{x}_i$ denotes the position of satellite i, $\mathcal{A} = +, \times$ denotes the GW polarization, $\tilde{h}_{\mathcal{A}}(f,\hat{k})$ is the Fourier transform of the GW signal, f is the GW frequency, $\hat{k}$ the outward vector in the direction of the incoming GW and $\mathrm{d}\Omega_{\hat{k}}$ is the infinitesimal solid angle.
The above expression quantifies the fractional frequency shift due to a superposition of plane waves coming from different directions $\hat{k}$.
The term $\xi_{ij}^{\mathcal{A}}$ projects the incoming wave with polarization $\mathcal{A}$ onto the detector, and its functional dependence is given by:

$$\xi_{ij}^{\mathcal{A}}\left(f,\hat{k}\right) = e^{-2\pi i f \hat{k}\cdot\vec{L}_{ij}} \mathcal{M}_{ij}(f,\hat{k})\, \mathcal{G}^{\mathcal{A}}(\hat{k},\hat{l}_{ij})\,, \tag{25}$$

where

$$\mathcal{M}_{ij}(f,\hat{k}) \equiv \mathrm{e}^{\pi i f L_{ij}(1+\hat{k}\cdot\hat{l}_{ij})}\ \mathrm{sinc}\left(\pi f L_{ij}(1+\hat{k}\cdot\hat{l}_{ij})\right) \tag{26}$$

and

$$\mathcal{G}^{\mathcal{A}}(\hat{k},\hat{l}_{ij}) \equiv \frac{\hat{l}^a_{ij}\hat{l}^b_{ij}}{2} e^{\mathcal{A}}_{ab}(\hat{k})\,, \tag{27}$$

where $\hat{l}_{ij} = (\vec{x}_j - \vec{x}_i)/|\vec{x}_j - \vec{x}_i|$ is a unit vector pointing from spacecraft i to j and $e^{\mathcal{A}}_{ab}(\hat{k})$ denotes the GW polarization tensors.

For an a homogeneous, isotropic and non-chiral, stochastic background, the GW signal is only specified statistically

$$\langle \tilde{h}_{\mathcal{A}}(f,\hat{k})\, \tilde{h}^*_B(f',\hat{k}')\rangle = \delta(f-f')\delta(\hat{k}-\hat{k}')\delta_{\mathcal{A}B}\frac{P_h^{\mathcal{A}B}(f)}{16\pi}$$

and

$$\langle \tilde{h}_{\mathcal{A}}(f,\hat{k})\, \tilde{h}_B(f',\hat{k}')\rangle = 0\,.$$

Homogeneity and isotropy implies that $P_h^{\mathcal{A}B}(f)$ is diagonal, whereas the non-chirality implies $P_h^{\times\times} = P_h^{++}$, so that we can define $P_h := \sum_{\mathcal{A}} P_h^{\mathcal{A}\mathcal{A}}$.

We characterise the response of the individual links to a stochastic background statistically

$$\langle \tilde{\eta}^{GW}_{ij}\, \tilde{\eta}^{GW}_{mn}\rangle = \frac{1}{2} S^{\eta,\mathrm{GW}}_{ij,mn}(f)\delta(f-f')\,, \tag{28}$$

where spectral densities for the link measurements are given by

$$S^{\eta,\mathrm{GW}}_{ij,mn}(f) = \frac{f^2}{f_{ij}f_{mn}} e^{-2\pi i f(L_{ij}-L_{mn})} \sum_{\mathcal{A}} P_h^{\mathcal{A}\mathcal{A}}(f)\; \Upsilon^{\mathcal{A}}_{ij,mn}(f)\,, \tag{29}$$

with:

$$\Upsilon^{\mathcal{A}}_{ij,mn}(f) = \int \frac{\mathrm{d}\Omega_{\hat{\mathrm{k}}}}{4\pi}\, \mathrm{e}^{-2\pi i f \hat{k}\cdot(\vec{x}_i - \vec{x}_m)}\; \xi^{\mathcal{A}}_{ij}(f,\hat{k})\, \xi^{\mathcal{A}}_{mn}(f,\hat{k})^*\,. \tag{30}$$

The power spectral densities of the signal in the TDI variables described in sec. II D can then be computed from

$$\begin{aligned}\langle \tilde{U}(f)\tilde{V}^*(f')\rangle &= \frac{1}{2} S^{\mathrm{GW}}_{UV}(f)\delta(f-f') \\ S^{\mathrm{GW}}_{UV}(f) &= \sum_{ij,mn\in\mathcal{I}} c^U_{ij}(f) c^{V*}_{mn}(f) S^{\eta,\mathrm{GW}}_{ij,mn}(f)\,,\end{aligned} \tag{31}$$

where $\tilde{U}$ and $\tilde{V}$ denote any two TDI variables, which in our case are TDI A, E and ζ, and $\mathcal{I} = \{12, 13, 23, 21, 31, 32\}$ denotes the set of pairs of indices that define the six inter-satellite links. The coefficients $c^U_{ij/mn}$ map the single-link measurements onto the TDI variable U. Refer to the Mathematica code for the computation of such coefficients (noise-analytical-model).

Note that considering each polarization of the SGWB contributes equally to the background, i.e. $P_h^{\times\times} = P_h^{++}$, we can rewrite Eq. (31) as a product of the SGWB spectral density $P_h(f)$ and a transfer function $\mathcal{T}^{GW}(f)$ which takes into account the LISA detector response, i.e. $S^{\mathrm{GW}}_{UV}(f) = \mathcal{T}^{GW}(f)P_h(f)$. $S^{\mathrm{GW}}_{UV}(f)$ would correspond to the first term on the right hand side of Eq. (6). The transfer functions for the three TDI channels and their cross correlation are shown in Fig.5.

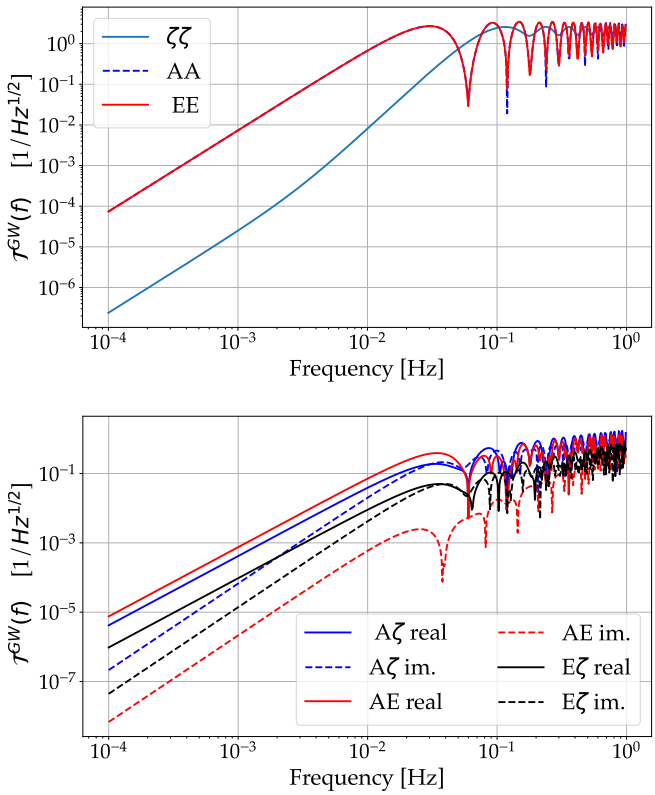

FIG. 5. Upper panel: Gravitational wave transfer functions $\mathcal{T}^{GW}(f)$ of the three time delay interferometry channels A,E and ζ assuming a constellation of three fixed unequal arm-lengths; lower panel: real and imaginary components of the gravitational wave transfer functions $\mathcal{T}^{GW}(f)$ of the time delay interferometry channels AE, Eζ,Aζ.

F. SGWB Signal models

There are a large variety of models for stochastic gravitational wave backgrounds that might manifest in the LISA band [1]. In this work we focus on four models, which can be described by their energy density, $h^2\Omega_{GW}$ [15], which is a function of some parameters, θ:

- **Power law**:

$$h^2\Omega_{GW}(f) \approx A\left(\frac{f}{f_p}\right)^n\,, \tag{32}$$

where f_p is the pivot frequency, defined as the geometrical mean of the LISA frequency interval

(10^{-4} Hz, 0.1 Hz), f_p = 3mHz. The model parameters are the log-amplitude, A, and slope, n [7, 30]. We use reference values of $n = 2/3$ and $A = 7.87 \times 10^{-13}$, representing a SGWB from stellar origin black hole binaries that has energy density at 1mHz of $h^2\Omega_{GW}(1mHz) = 3.78 \times 10^{-13}$. This value was chosen to be compatible with LIGO-VIRGO-KAGRA constraints [7]

- **Gaussian bump**:

$$h^2\Omega_{GW} = Ae^{-\frac{1}{2\sigma^2}\ln(\frac{f}{f_p})^2}, \tag{33}$$

where f_p is the pivot frequency as before. The model parameters are the log-amplitude, A, and width, σ. We use reference values of $A = 10^{-12.48}$ and $\sigma = 0.3$ whose energy density at 1mHz is $h^2\Omega_{GW}(1mHz) = 4.05 \times 10^{-16}$. This signal is chosen as a simple way to mimic the one which might arise from particle production taking place for a limited number of e-folds during inflation (as, for instance, required by some models of primordial BH generation). (See e.g. [11, 12, 21])

- **Power law with running:**

$$h^2\Omega_{GW} = A\left(\frac{f}{f_p}\right)^{n+\alpha\ln(\frac{f}{f_p})}, \tag{34}$$

where f_p is the pivot frequency as before. The model parameters are the log-amplitude, A, the slope, n, and the running index, α. We use reference values of $A = 10^{-12.65}$, $n = 1$ and $\alpha = -0.1$. This signal is motivated by non-standard inflationary models. For example, gravitational wave generation can be enhanced by sustained particle production during inflation, leading to a power law stochastic GW background, which would deviate from a simple power law at higher frequency when back-reaction kicks in (see e.g. [13]). The energy density at 1mHz is $h^2\Omega_{GW}(1mHz) = 6.61 \times 10^{-14}$

- **First Order Phase Transition**:

$$h^2\Omega_{GW}(f) = h^2\Omega_p\left(\frac{f}{f_p}\right)^3\left(\frac{7}{4+3\left(\frac{f}{f_p}\right)^2}\right)^n, \tag{35}$$

where $f_p = 2 \cdot 10^{-4}$ Hz (note this is different to the reference frequency in the previous models). The model parameters are the energy density, $h^2\Omega_p$, and spectral index, n. We use reference values of $A \equiv h^2\Omega_p = 10^{-10}$ and $n = 7/2$ whose energy density at 1mHz is $h^2\Omega_{GW}(1mHz) = 2.59 \times 10^{-12}$. This signal is motivated by the production of sound waves in the cosmic fluid from colliding phase transition bubbles [17, 28].

In our analysis, we also include the contribution to the spectral density from the foreground of galactic binaries (GB). We use the following model for the foreground [1]:

- **Foreground of Galactic Binaries**:

$$S_{GB}(f) = A_{GB}\left(\frac{f}{Hz}\right)^{-\frac{7}{3}} e^{-(f/f_1)^\alpha} \times \frac{1}{2}\left[1 + \tanh\left(\frac{f_{knee} - f}{f_2}\right)\right] \tag{36}$$

with:

$$f_1 = 10^{a_1 \log_{10}(T) + b_1}, f_{knee} = 10^{a_k \log_{10}(T) + b_k}$$

.

setting $A = 1.15 \cdot 10^{-44}$; $\alpha = 1.56$; $a_1 = -0.15$; $b_1 = -2.72$; $a_k = -0.37$; $b_k = -2.49$; $f_2 = 6.7 \times 10^{-4}$Hz. When considering the background in conjunction with other SGWBs we allow the amplitude to vary, but keep the other parameters fixed.

The relation between the energy density Ω_{GW} and the stochastic GW background power spectral density $P_h(f)$ is given by [15]:

$$\Omega_{GW}(f) = \frac{4\pi^2}{3H_0^2} f^3 P_h(f), \tag{37}$$

where H_0 is the Hubble constant fixed to be 67.8 km/s/Mpc, as a consequence $h = 0.678$. The conversion between the energy density $\Omega_{GW}(f)$ and gravitational power spectral density $P_h(f)$ used to compute Eq.(31) is then [15]:

$$P_h(f) = 7.98 \times 10^{-37}\left(\frac{Hz}{f}\right)^3 h^2\Omega_{GW}(f)\frac{1}{Hz}, \tag{38}$$

.

We report in Fig. 6 the ASD of the four SGWB models together with the ASD of the reference instrumental noise in TDI channel A. [9]

We also provide the computation of the SNRs of these different backgrounds in the TDI channel A using the following formula [44]:

$$SNR_A = \sqrt{T}\left[\int_0^\infty \frac{S_{AA}^{GW}(f)^2}{S_n^A(f)^2} \mathrm{d}f\right]^{1/2} \tag{39}$$

with an observation time span of $T = 4$ years. Here $S_{AA}^{GW}(f)$ is the spectral density in channel A that can be computed from Eq. (31) and S_n^A is the PSD of the A channel. The results[2] are shown in Table I.

[2] We note that this formula is derived assuming that we have access to two independent channels that have uncorrelated noise and perfectly correlated signals. This is not a good approximation to LISA, so the SNR is not directly interpretable. However, it still provides an indication of the relative detectability of different backgrounds.

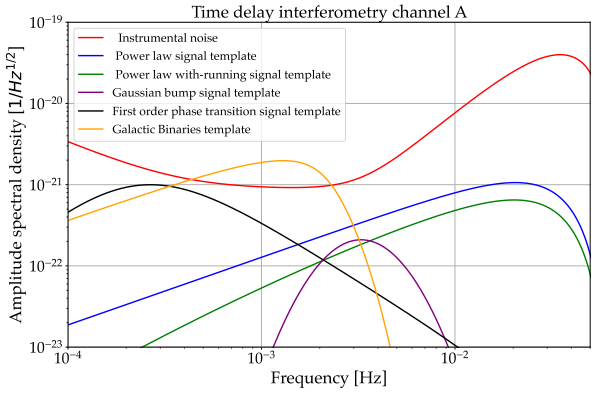

FIG. 6. Amplitude spectral density of the stochastic GW background models and the amplitude spectral density of the reference test mass and optical metrology noise in the time delay interferometry channel A.

SGWB Model	SNR w/o GB	SNR w/ GB
Power law with running	14.54	13.35
Power law	48.70	42.89
Gaussian bump	13.51	11.65
First order phase transition	118.68	64.18

TABLE I. Signal to noise ratio in TDI channel A for the four SGWB models, with and without the presence of the galactic foreground as an additional noise component. The galactic foreground here considered has an SNR of 1627.39

It is possible to notice that including the foreground as part of the noise ($S_n^A(f) := S_{GB}^A(f) + S_n^A(f)$) leads to a substantial decrease of the SNR for the FOPT background but the SNR does not change very much for the other models.

We plot in fig. 7 the value of the SNR in channel A vs. the energy density at 1mHz for the different models. The dotted lines assume no presence of the foreground, whereas the continuous lines include the presence of the foreground. As expected there is a direct correlation between increasing the energy density and an increase in the SNR. Moreover, the presence of the foreground mostly affects the SNR of the FOPT. In fact, in the presence of the foreground the energy density must be two times larger to have the same SNR as it would in the absence of a foreground.

III. RESULTS

A. Impact of instrumental noise knowledge uncertainty on SGWB recovery

Here, we explore how the measurement precision of the SGWB parameters changes in the presence of instrumental noise knowledge uncertainty, for each of the SGWB models described in Section II F. We use the Fisher matrix formalism described in Section II B, which assumes

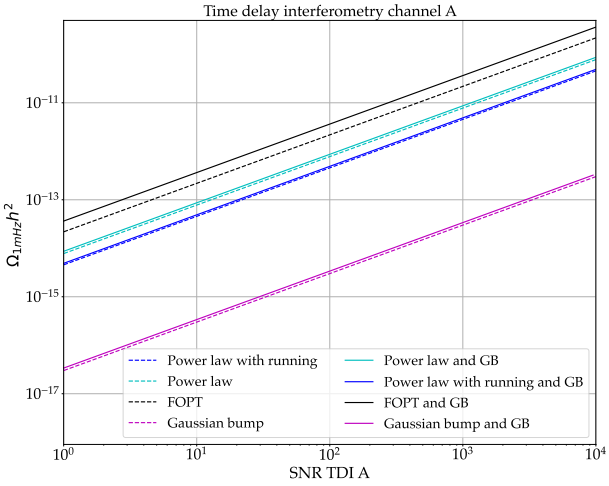

FIG. 7. Signal to noise ratio of four different SGWB signals in the TDI channel A, Power law, Power law-with-running, Gaussian bump and First order phase transition, versus the energy density at 1mHz, both considering (continuous lines) or not (dashed lines) the presence foreground

that the noise is uncorrelated at different frequencies. We assume we use three TDI channels in our analysis, A, E and ζ, as described in Section II D. We model uncertainties in the PSD and CSD at each frequency following the model described in Section II C. To build the Fisher matrix we need the following elements:

1. The derivatives of the PSD and CSD at each frequency with respect to the parameters of the SGWB model.

2. The derivatives of the PSD and CSD at each frequency with respect to the parameter (amplitude) of the Galactic Binaries. The addition of this parameter extends the dimension of the Fisher matrix by one.

3. The derivatives of the PSD and CSD at each frequency with respect to the parameters of the instrumental noise model. The instrumental noise model is based on 9 different splines: 3 splines to model the PSD of A, E and ζ, and 3 splines each for real and imaginary parts of the CSDs for AE, Aζ and Eζ. Each spline has a number of parameters equal to the umber of knots, which we take to be 13. The total number of noise parameters is therefore 9 x 13 = 117.

4. The evaluation of the Fisher matrix from these elements using Eq. (9), which is summed over frequency.

5. The choice of a prior on the instrumental noise parameters. We use a Gaussian prior, which is implemented in the Fisher matrix formalism by adding the prior matrix to the Fisher matrix before computing its inverse (see Eq. (11)). For this first study

we take the priors on each noise parameter to be independent, with zero mean and equal variance, $\sigma_{\rm inst}$. In this section we fix $\sigma_{\rm inst} = 1$, which means we are allowing for up to an order of magnitude uncertainty in the instrumental noise at each frequency.

6. We compute the inverse of the Fisher matrix after adding the prior to obtain an estimate of the measurement uncertainty, from the square root of the diagonal elements of the inverse as explained in Sec. II B. We also compute the inverse of the SGWB-parameter only sub-matrix of the Fisher matrix, which represents the expected uncertainty in the absence of instrumental noise uncertainties.

For each SGWB model we will present the results in two different ways. Firstly, we will show the ratio of the uncertainties in the SGWB parameters in the presence of instrumental noise uncertainties to those uncertainties when perfect knowledge of the instrumental noise is assumed. These results illustrate the impact of lack of noise knowledge on SGWB characterisation. Secondly, we will show the actual uncertainties in the SGWB parameters, as computed from the Fisher matrix. Of particular interest is the uncertainty in the log-energy density of the background. As a rule of thumb, a background will be detectable if the uncertainty $\Delta \ln(A) < 1$ ($\Delta \ln(A) = (\Delta A)/A$). In both cases, we will plot results as a function of the background amplitude/the background energy density at a reference frequency of 1mHz (the logarithm of these quantities are linearly related, so they can be easily represented using bottom/top axes in a single figure). For the second type of plot, solid lines show results in the presence of noise knowledge uncertainty, and dashed lines give results assuming perfect noise knowledge. In both the analysis we consider the foreground amplitude to vary and we consider it as additional source of noise together with the instrumental noise.

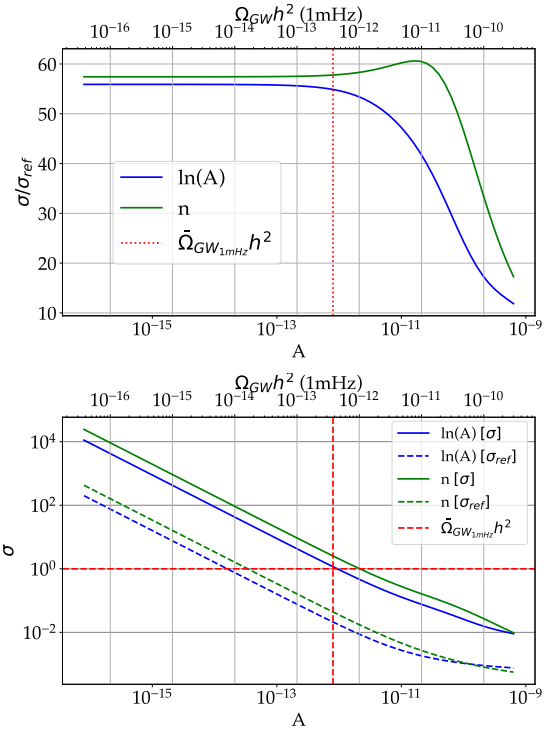

FIG. 8. Results for the power law SGWB model considering the foreground as additional source of noise. The upper panel shows the ratio of the uncertainties of the SGWB parameters (amplitude and slope) when including instrumental noise uncertainties or assuming perfect noise knowledge. This ratio is plotted versus the amplitude (bottom axis) and SGWB energy density at 1mHz (top axis). The lower panel shows the estimated parameter uncertainties for the two cases. Once again this is as a function of amplitude/energy density, but for a restricted range. The horizontal red dashed line corresponds to an uncertainty of one, which is our threshold on the uncertainty in log-energy density for deciding that a background is detectable. The vertical red dashed line indicates the reference SGWB amplitude given in Section II F.

1. *Power law*

A power law SGWB is described by two parameters: the slope and the amplitude. The full Fisher matrix, including instrumental noise and foreground parameters, is 120×120. Figure 8 shows the results computed for this model. We see that in the presence of instrumental noise uncertainties, the uncertainty in the SGWB parameters increases by a factor of $\sim$ 55–60, with the uncertainty in the slope being slightly more affected than that of the amplitude. The increase is lower for high background amplitudes, as expected, but only when the background is one to two orders of magnitude brighter than the reference value. Considering the raw uncertainties, we see that the uncertainty in the log-energy density is typically a factor of $\sim$ 50 larger and the background energy density would have to to be a factor of $\sim$ 50 times higher to be characterised with the same measurement precision when there is instrumental noise uncertainty as it could be without those uncertainties. However, a background with amplitude equal to the reference value should (just) be detectable even allowing for confusion with instrumental noise mismodelling.

2. *Power law with running*

For the power law with running SGWB, the fisher matrix is 121×121, as the SGWB model depends on 3 parameters: slope, amplitude and running index, α. The results for this model are shown in fig. 9. In this case we see that the uncertainties in the SGWB parameters increase by a factor of $\sim$ 30–75, with the uncertainty on the amplitude being most affected in this case. Once again, the relative increase in the uncertainty is somewhat lower at higher background amplitudes. The lower

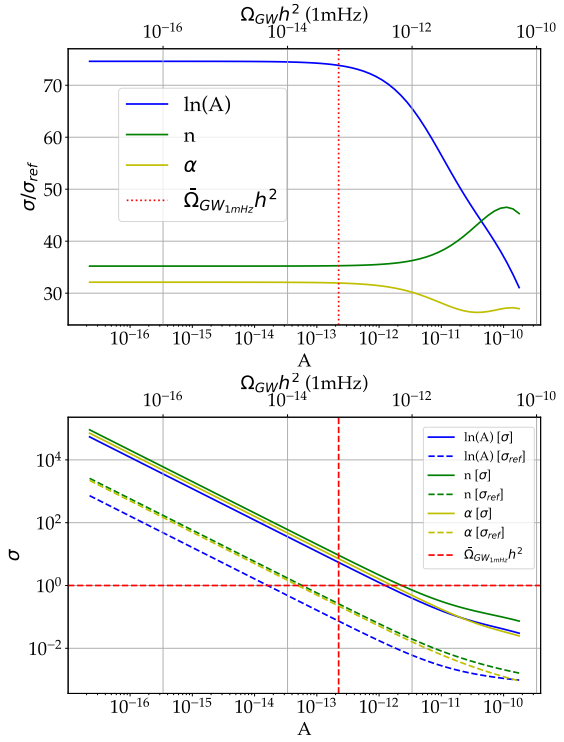

FIG. 9. As Figure 8, but now for the power-law with running SGWB model

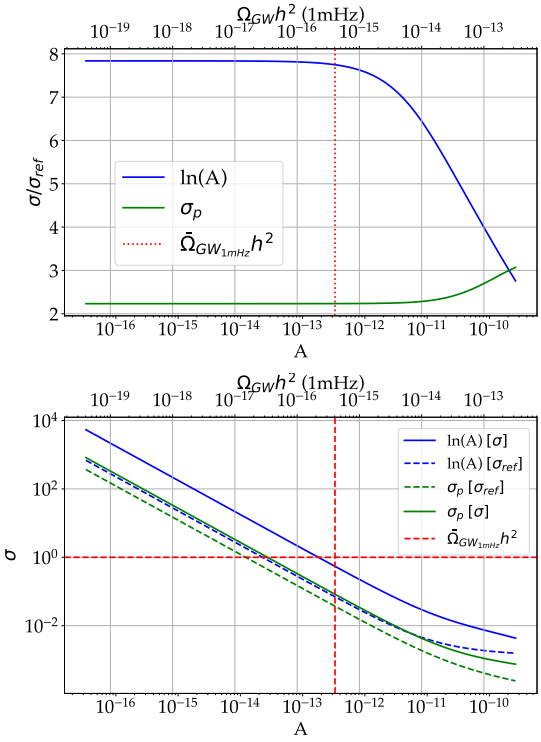

FIG. 10. As Figure 8, but now for the Gaussian bump SGWB model

panel of fig. 9 shows that the background is not detectable at the reference amplitude. An energy density ~ 20 times higher would be required for a detection. In general, the background has to have an energy density ~ 60 times higher to be characterised with the same measurement precision when there is instrumental noise uncertainty as it could be without those uncertainties and there is a similar increase in the parameter measurement uncertainty at fixed background energy density.

3. *Gaussian bump*

As for the power law, the Fisher matrix is a 120×120 as we have 2 signal parameters: the Gaussian width and the amplitude. The results for this model are shown in Figure 10. In this case, the degradation in the precision of parameter measurement is a factor of $\sim$ 2–8 when allowing for lack of knowledge of the instrumental noise. This difference in behaviour is related to the different shapes of the SGWBs being considered. A Gaussian is more distinct from the spline model being used to represent the instrumental noise uncertainties than a power law, and hence the degree of confusion between the two models is less in this case. From the lower panel of Figure 10: we see that the energy density in a Gaussian bump SGWB has to be a factor of ~ 10 times higher for it to be characterised with the same measurement precision when there is instrumental noise uncertainty as it could be in the absence of those uncertainties. A Gaussian bump background at the reference amplitude would be detectable, and the width of such a Gaussian could be measured to a few tens of percent precision. This measurement precision improves approximately linearly with the background energy density.

4. *First order phase transition*

The FOPT model is again characterised by two parameters, an amplitude and a spectral index, and has a 120×120 Fisher matrix. The results for this model are shown in Figure 11. When allowing for instrumental noise knowledge uncertainties, the precision with which the SGWB log-energy density can be characterised degrades by a factor of ~ 20. The degradation in the determination of the spectral index is even larger, ~ 35. Once again, to achieve the same measurement precision, the background energy density would have to be ~ 20 times larger than it would need to be in the absence of noise knowledge uncertainties. Nonetheless, a FOPT background at the reference amplitude would still be detectable and provide a measurement of the spectral index at the level of $\sim \pm 0.8$.

The previous results were computed considering the presence of the galactic foreground. In the appendix C we report similar results, computed without taking into consideration the Galactic foreground. Redoing

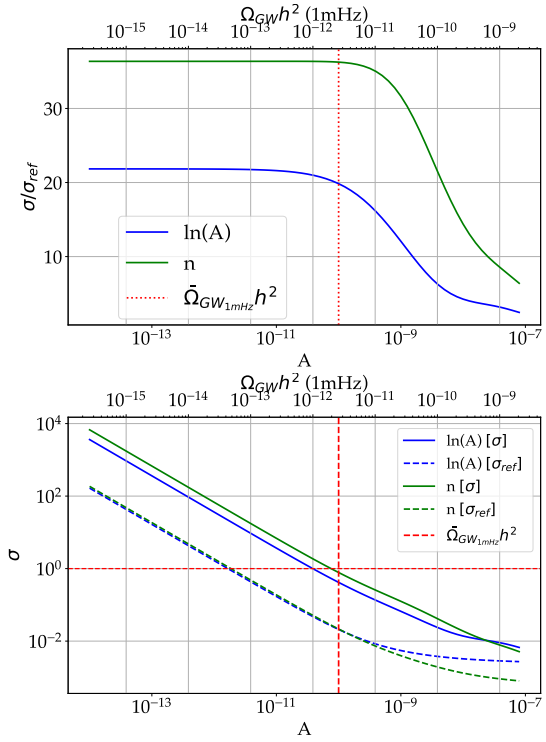

FIG. 11. As Figure 8, but now for the first order phase transition SGWB model

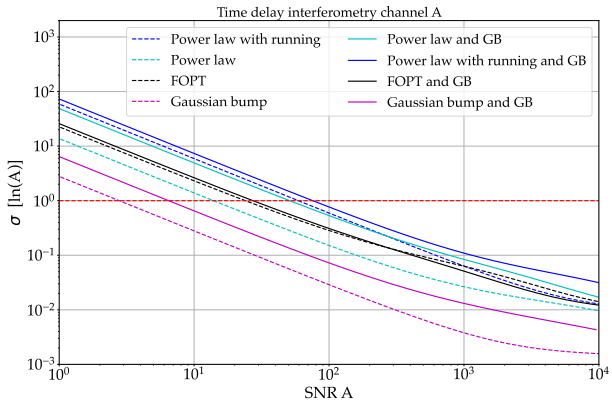

FIG. 12. Signal to noise ratio of four different SGWB signals in the TDI channel A, Power law, Power law-with-running, Gaussian bump and First order phase transition, versus the error in log amplitude both considering (continuous lines) or not (dashed lines) the presence foreground

these analyses ignoring the foreground we do not see big differences in the uncertainty ratio, nor in the absolute uncertainties, when these are compared at fixed SNR, i.e., when the signal-to-noise ratio is recomputed without the galactic binaries included in the spectral density. To illustrate this, we show in Fig.12 the precision of the measurement of the log-energy density of the background, as a function of the SNR in TDI channel A, for all SGWB models and both including and not including the galactic binary foreground. We see that the uncertainty is typically larger when the foreground is present, but this is typically less than a factor of a few. The Gaussian bump and power law background are most affected, with the uncertainty at fixed SNR and the SNR required for detection both decreasing by a factor of a few when the galactic binary background is removed from the spectral density. For the Gaussian bump, the uncertainty decreases by a factor of a little more than two when the Galactic background is excluded, and the SNR needed to reach the $\Delta \ln(A) < 1$ threshold for detection decreases by a similar factor. For the power law, the uncertainty decreases by about a factor of 4, and the $\Delta \ln(A) < 1$ threshold required for detection is reached at an SNR that is a factor of ~ 4 smaller. For the power law with running and the FOPT backgrounds, the uncertainty at fixed SNR is almost unchanged, and the threshold SNR for detection is within a factor of 1.5 and 2, respectively.

This behaviour can be understood by looking at the shapes of the various SGWBs in Figure 6. Figure 7 demonstrates that the removal of the foreground does not affect the SNR very much. The only SGWB that shows a significant change is the FOPT, for which most of the power is at frequencies where the foreground is significant. However, in the region around 300μHz, where the majority of the SNR is generated, the shape of the FOPT is very different to the foreground. This is also true for the power-law-with running model around 5mHz, where the majority of its SNR is generated. The power-law model, on the other hand, is quite parallel to the foreground at low frequency, and the Gaussian bump is quite parallel to the foreground at a few mHz. This most likely explains why the latter two backgrounds are more difficult to distinguish from a galactic foreground, and therefore more affected by its inclusion.

B. Setting a noise knowledge requirement

In this section we will now explore how the amount of uncertainty in the instrumental noise impacts the results. In practice we will not be completely ignorant of the instrumental noise. Measurements on-board the satellites will provide an indication of the size of certain noise components. In principle, it might therefore be possible to place a requirement on how well the instrumental noise must be known in order to not degrade the science output of the mission. To assess this, we will recompute the results while changing the variance of the Gaussian prior on the instrumental noise spline parameters. We will vary the prior on the spline weights from very small values ($\log_{10}(\sigma_{inst}) = -10$), representing near-perfect knowledge of the noise, to very high values $\log_{10}(\sigma_{inst}) = 6$, representing no knowledge of the noise.

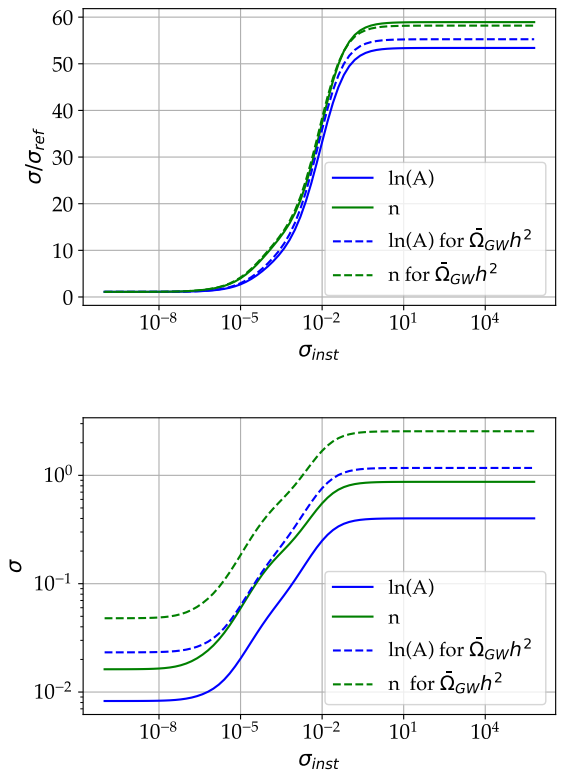

FIG. 13. As Figure 8, but now for fixed background amplitude and varying the variance of the Gaussian prior on the instrumental noise spline model. This plot is for a power law background, and the amplitude has been fixed such that the SNR in TDI channel A is 138 (continous line) and 43.7 (dashed lines).

We fix the amplitude of the background for each SGWB model, so that it corresponds to an SNR of $\sim 120 - 140$ in each case [3]. This choice of SNR was motivated by Figure 12, which shows that an SNR greater than 100 is required in order to ensure all types of SGWB are detectable. For the case of the power law we also show results with the amplitude set to the reference energy density, which shows that the exact choice of background amplitude does not make a significant difference to the qualitative behaviour, only to the absolute value of the uncertainty.

For all SGWB models we again present the results in two different ways — as a ratio of the SGWB parameter measurement uncertainties when instrumental noise uncertainties are considered to those assuming perfect noise knowledge, and as the absolute measurement uncertainty. Results for the power law model are shown in Figure 13, for the Power-law-with-running model in Figure 14, for the Gaussian bump model in Figure 15 and for the FOPT in Figure 16. The results for all four SGWB models are qualitatively similar. For very low prior uncertainties the ratio of the uncertainties tends to unity. This is expected as this limit corresponds to the limit in which the instrumental noise is perfectly known. As the prior uncertainty is increased beyond $\sim 10^{-6}$ the measurement precision in the presence of noise knowledge uncertainties starts to increase. When the noise knowledge uncertainty reaches $\sim 10^{-2}$ for power law and Gaussian bump, $\sim 10^{-1}$ for power law-with-running and 10 for FOPT, the measurement precision ratio saturates. This final value reflects the expected uncertainty in the absence of any noise knowledge. The results given in Section III A were all computed in this regime.

The main conclusion from these results is that if we wanted to ensure that there was no degradation in LISA science due to lack of noise knowledge, the necessary requirement on the noise knowledge would be $<<$ 10%. In the LISA Pathfinder mission, which was designed to accurately characterize the free-fall performance of test masses in a space-based environment, the observed noise could only be explained within some margin: the physical origin of the measured sub-mHz acceleration is only partially understood, as more than 50% of its PSD is still unmodeled [19, 41].

It is therefore unrealistic to expect that a noise requirement at the $\sim$ 1–10% level could be met. At noise uncertainties above this threshold, there is little difference between some and no noise-knowledge, at least within the model for instrumental noise variations considered here. We conclude that no useful and achievable noise knowledge requirement could be implemented in practice.

While we will not be able to achieve the precision that would be possible under ideal circumstances, it is important to emphasise that this does not mean we will not be able to detect and characterise modelled SGWBs. In all cases, at SNR of $\sim>$ 100, the amplitude can be constrained to a few tens of percent, even without any knowledge of the instrumental noise.

C. Signal reconstruction

To finish this section we will use our Fisher matrix results to illustrate how well we can reconstruct the Power law, the foreground, and the instrumental noise. To do this, we will approximate the posterior distribution on the model parameters using a multi-variate Gaussian with covariance matrix equal to the inverse of the Fisher matrix. We can then take random draws from this fake[4] posterior distribution and plot the PSD

[3] Specifically the SNR of the power law with running is 135, the SNR of the power law is 138, the SNR of the FOPT is 142 and the SNR of the Gaussian bump is 120.

[4] Even if the measurements x are Gaussian the posterior is not because is a function of θ. A Gaussian with unknown variance σ

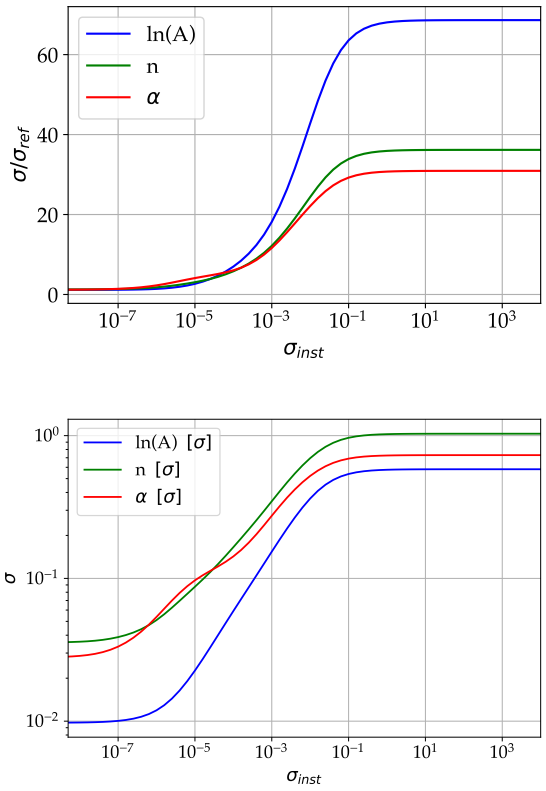

FIG. 14. As Figure fig. 13 but now for the power-law-with-running model. The background amplitude has been fixed to give an overall SNR of 135.

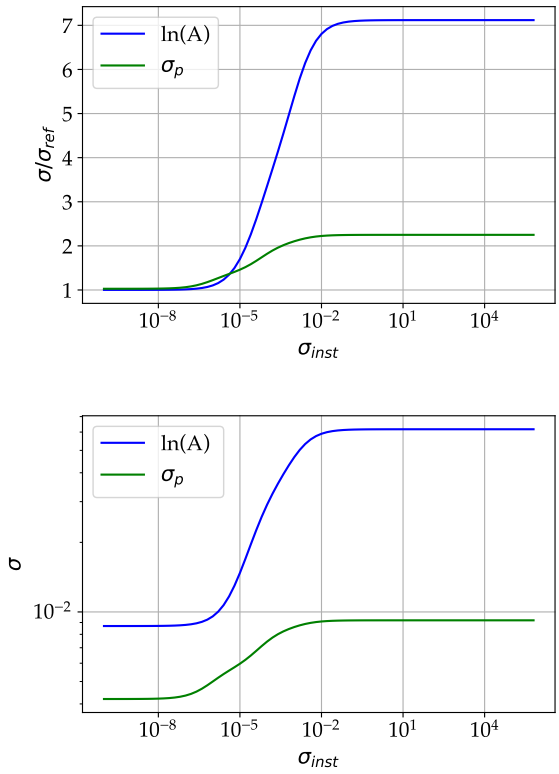

FIG. 15. As Figure fig. 13 but now for the Gaussian bump model. The background amplitude has been fixed to give an overall SNR of 122.

of the SGWB, the foreground and instrumental noise corresponding to the drawn parameters. In fig. 17 we follow this procedure for a power law signal with an SNR of 872. The choice of the SNR is driven to avoid the breakdown of the Fisher matrix approximation for the SGWB parameters, because the SGWB parameter uncertainties are large and no longer in the linear signal regime as explained and, shown in details, in Appendix C 1.

The three panels show the reconstructed ASDs for the Power law, for the foreground and for the instrumental noise and the total, which is the sum of the three.

What we would expect is that our ability to measure the total spectral density is roughly independent of the relative amplitudes of the two components, since this is what we actually see and measure in the data. Our model attempts to split that measurement into constituent components. If one of those components is much weaker than the other we would not expect to recover it as well as when the components are making comparable contributions to the data. Top panel of Fig. 17 (and the Figure 26 in the appendix C 1) is consistent with this expectation. We see indeed in Fig. 17 that the galactic binaries are well recovered. Moreover, the only noise reconstruction for the TDI A and E suffers from the presence of the GW background and foreground in the regime $0.4mHz$ – $4mHz$ where these two signals have the majority of power. As a final point, it is clear that the SGWB is being best constrained around a frequency of 4mHz where the power of the GB is less and the uncertainty in the instrumental noise is also largest (although still small) at this point. This can be understood from Figure 6, which shows that the power law background is closest to the instrumental noise ASD at that frequency and the Galactic binaries pick at 1mHz, and so this frequency range dominates the SNR in the signal. We expect to be able to measure the background best in the frequency range where it is most dominant relative to the instrumental noise and distinguishable from the galactic binaries.

IV. DISCUSSION AND CONCLUSION

We have explored the impact of noise knowledge uncertainty on measuring the parameters of various mod-

is not a Gaussian on that variance, $p(x|\theta) \propto \frac{1}{\sigma}\exp(-\frac{x^2}{2\sigma^2})$, is a Gaussian in x, but not in σ

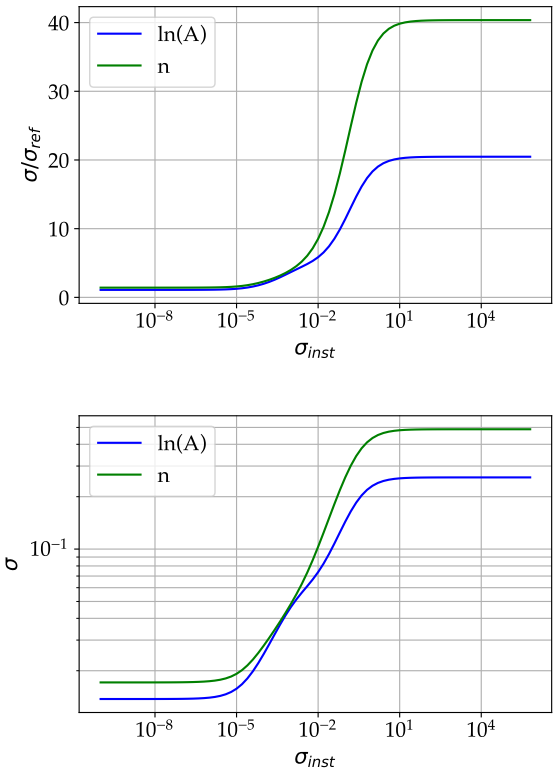

FIG. 16. As Figure fig. 13 but now for the FOPT model. The background amplitude has been fixed to give an overall SNR of 142.

elled stochastic gravitational wave backgrounds. This was done by modelling instrumental noise uncertainties using cubic splines to represent deviations away from the design PSDs and CSDs for the three TDI channels A, E and ζ. We then used a Fisher matrix analysis to evaluate the expected uncertainties in the measurements of the model parameters when fitting a model including the instrumental noise uncertainties and compared it to fitting a model without those uncertainties. The degree of uncertainty was characterized by including a Gaussian prior on the instrumental noise parameters, allowing us to quantify the impact of imposing a requirement on our noise knowledge.

This analysis showed that, for all SGWB models, allowing for instrumental noise uncertainties leads to a significant increase in the uncertainty in our measurements of the background parameters. The increase in uncertainty was a factor of $2-8$ for the Gaussian bump model, which reduces to $2-4$ when not including GB as foreground, $55-60$ for the power law ($15-30$ without GB as foreground), $20-35$ for the First order phase transition ($20-50$ without GB as foreground) and $30-75$ for the power law with running ($20-75$ without GB as foreground). These increased uncertainties correspond to the threshold background energy density required for detection increasing by a factor of 10 (5 without GB)

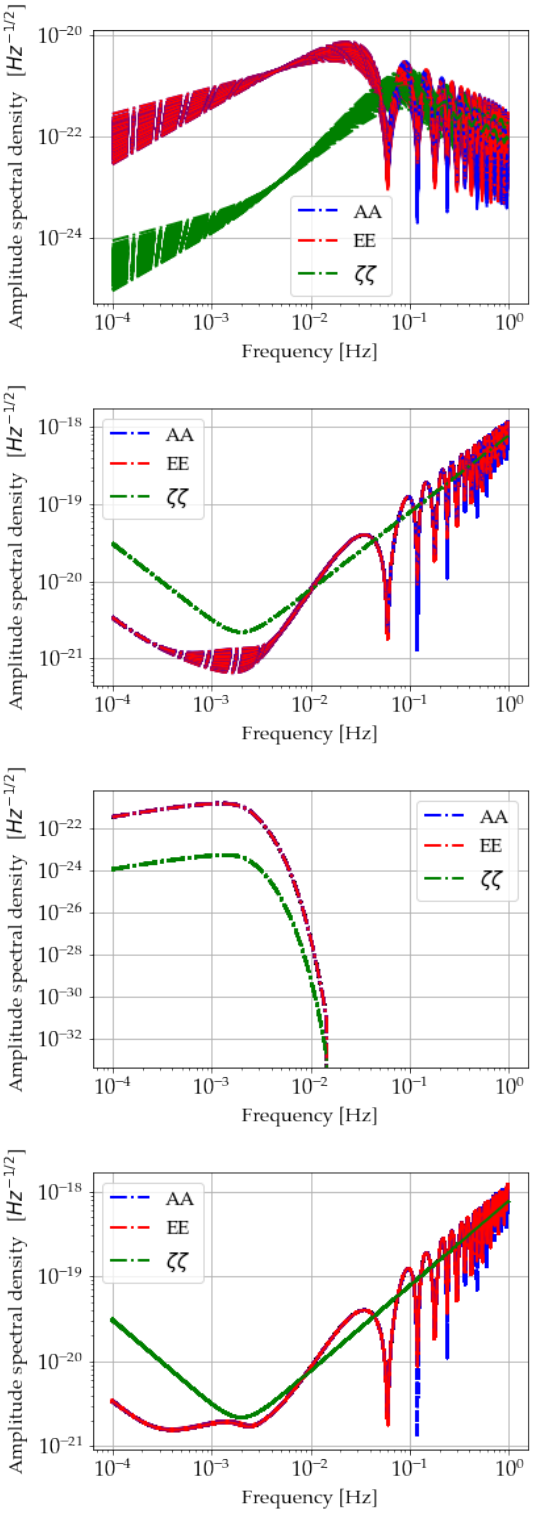

FIG. 17. We show the Power law signal, Galactic binaries and noise ASDs corresponding to random draws from the posterior, approximated using the Fisher matrix as described in the text. In each panel the curves correspond to the three TDI channels: A (blue), E (red) and ζ (green). Upper first panel: reconstructed SGWB; upper second panel: reconstructed TM and OMS instrumental noise; middle panel: reconstructed Galactic binaries; lower panel: total reconstructed ASD (signal + noise + GB).

for the Gaussian bump model, a factor of 60 with and without GB for the Power-with-running and a factor of 20 with and without GB for all other models (50 for the power law when including GBs). The threshold energy density at 1mHz at which the backgrounds start to be detectable are 4×10^{-13}, 4×10^{-13}, 2×10^{-16} and 10^{-12} (10^{-13}, 2.5×10^{-13}, 8×10^{-17} and 5×10^{-13} if we do not include the GB foreground) for the power law, power law with running, Gaussian bump and FOPT models respectively. Comparing these to the reference background amplitudes introduced in Section II F we see that the power law, the Gaussian bump and FOPT backgrounds are detectable at the reference amplitudes, while the power law with running is not as the threshold energy density is 1.5 times higher than the reference. However, for this latter background the amplitudes were specified based on the SNR and not on a physical model. The reference amplitudes for the power law and FOPT backgrounds are based on physical model predictions, so it is more important that these backgrounds are still detectable. We note that this result does depend on the particular choice of model we used for representing the instrumental noise uncertainty. If this model is made even more flexible, for example by increasing the number of spline knots used, the threshold would increase further and potentially also make the reference backgrounds undetectable.

When we vary our assumed level of knowledge of the instrumental noise, we find that the uncertainties on the SGWB parameters show a similar trend for all models, starting to degrade at relative small uncertainties, increasing and then saturating after a certain point. The point at which the sensitivity starts to degrade is when the uncertainty in the log-spectral density of the noise reaches $\sim$ 10^{-6}–10^{-5}, depending on the SGWB model. The uncertainty saturates at log-spectral density uncertainties of $\sim$ $10^{-2}/10^{-1}/10^{-2}/10^{1}$ ($10^{-2}/10^{-1}/10^{-3}/10^{-1}$ in the absence of the GB foreground) for the power law/power-law with running/Gaussian bump/FOPT backgrounds respectively. This means that if we wanted to limit the degradation in the science that arises from lack of noise knowledge we would have to impose a very stringent requirement on our knowledge of the noise. This is likely to be impossible to implement in practice, so we will have to accept that our ability to resolve SGWBs will not be as good as calculations that assume perfect noise knowledge predict.

It is important to note that these results are based on some assumptions which might not hold in practice. In particular, we have considered only modelled SGWBs and we have assumed a particular form for variations in the PSD that forces variations to be smoothly varying as a function of frequency. If the number of knots is increased to obtain a more flexible instrumental noise model, with potentially faster variations of the PSD as a function of frequency, we already see a degradation of 2 or 3 orders of magnitude in the estimation of the log-energy density.
It is the distinguishability of the models that allows us to measure the parameters of the SGWBs. In the extreme picture where we do not want to make any assumption at all about the form of the instrumental or SGWB spectral densities, then spectral separation will not be possible. We will be able to report measured power spectral density in all channels, and cross-spectral densities between them, and translate these into upper limits on the SGWB amplitude; but any interpretation of this as an actual detection will require independent confirmation from another detector [33].

All previous studies of the separation of instrumental noise and stochastic backgrounds have required assumptions: in [10] it was assumed that the instrumental uncertainty is a spline and that the SGWB has a power law spectrum; in [26] it was assumed that the instrumental noise is determined by 12 individual noise levels; and in this paper we are assuming something similar to [10], although with a bit more flexibility, a wider variety of SGWB models and a different noise model for single satellite links. The SGWBinner [16] is agnostic on the spectrum of the background but it can only work because it assumes a specific model for the instrumental noise. That is not going to be possible in practice. SGWBinner could be adapted to use a more flexible noise model, similar to the model used here, but the precision on the background recovery will be degraded. If we have a completely general instrumental noise model and a completely general SGWB model then we won't be able to separate them. In that case, the only hope would be that the SGWB is above the design sensitivity and we trust that the instrumental noise meets the mission requirements, in which case the best interpretation of such an observation would be a SGWB. However, even then an assumption would be made that the mission had met the design sensitivity requirements. An exploration of how our ability to separate instrumental noise as the spectral models of the SGWB and the instrumental noise are made more complicated should be the focus of future work.

V. ACKNOWLEDGEMENT

M.M gratefully acknowledges the support of the German Space Agency, DLR. The work is supported by the Federal Ministry for Economic Affairs and Climate Action based on a resolution of the German Bundestag (Project Ref. No. FKZ 50 OQ 2301). The authors thank Chiara Caprini for her review and suggestions regarding the use of SGWB templates in the text. Additionally, we acknowledge Mauro Pieroni for providing feedback on the presented results and the implementation of spline models. Furthermore, we thank Olaf Hartwig for discussions on the accurate computation of the GW transfer function

and on the noise models and Marc Lilley for comparisons on the results obtained with the Fisher matrix formalism. We thank Lorenzo Sala for feedbacks on the recent analysis on the LISA Pathfinder performance results. The scientific discussions with Quentin Baghi, Jean Baptiste Bailey, Germano Nardini, Nikolaos Karnesis, Jesus Torrado, Nam Dam Quam, Henry Hinshauspe, Antoine Petiteau, and Riccardo Buscicchio have also been highly appreciated. Their feedback on the results and methodology presented in the paper has been valuable for the final outcome

Appendix A: Likelihood derivation

We derive the likelihood starting from the noise properties and explain why it takes the form shown in Sec. II. If we assume that the real time series $n(t)$ is a stationary, zero-mean, Gaussian and ergodic random process, then the Fourier transform of the noise $\tilde{n}_k = \tilde{n}(f_k)$ at each frequency f_k is normally distributed with zero-mean and variance σ_k^2. Thus, the natural log-likelihood at each frequency takes the form of a two-dimensional normal distribution

$$\ln p(\tilde{n}_k) = -\frac{1}{2}\Big(\frac{\Re[\tilde{n}_k]^2}{\sigma_k^2} + \frac{\Im[\tilde{n}_k]^2}{\sigma_k^2}\Big) - \frac{1}{2}\ln[(2\pi\sigma_k^2)^2] \quad \text{(A1)}$$

where we assumed that the real $\Re$ and imaginary $\Im$ part of the noise are not correlated and have the same variance. If we further assume that the variance of the noise at different frequencies follow a one-sided power spectral density $S_n(f)$ then :

$$< \tilde{n}^*(f')\tilde{n}(f) > = \frac{1}{2}S_n(f)\delta(f-f') \quad \text{(A2)}$$

$$< \tilde{n}(f')\tilde{n}(f) > = 0 \quad \text{(A3)}$$

where we used the expectation value of <> over the data generating process. For a set of frequencies the first relation can be written as

$$< \tilde{n}_k^*\tilde{n}_j > = \frac{T}{2}S_n(f_k)\delta_{jk} \quad \text{(A4)}$$

Therefore the variance of the real and imaginary part of the noise is given by

$$< \Re[\tilde{n}_k]^2 > = < \Im[\tilde{n}_k]^2 > = \frac{T}{4}S_n(f_k) = \sigma_k^2\,. \quad \text{(A5)}$$

We can write the natural log-likelihood for all the measured frequencies as:

$$\sum_k \ln p(\tilde{n}_k) = -\sum_{k=1}^{n}\ln[2\pi\frac{T}{4}S_n(f_k)] - \frac{1}{2}\sum_{k=1}^{n}\frac{|\tilde{n}(f)|^2}{\frac{T}{4}S_n(f_k)} \quad \text{(A6)}$$

which becomes in the continuum limit:

$$\ln p(\tilde{n}) = -\ln\left[2\pi\frac{1}{4}\det[S_n(f)\delta(f-f')]\right] - \frac{1}{2}4\int_0^\infty \frac{|\tilde{n}(f)|^2}{S_n(f)}\mathrm{df} \quad \text{(A7)}$$

Note that in the continuum limit the variance of the noise can be thought as an operator. In fact, one can define the inner product

$$(a(t)|b(t)) = 4\Re\int_0^\infty\int_0^\infty \tilde{a}^*(f)\,\Sigma^{-1}(f,f')\tilde{b}(f')\,\mathrm{df}\,\mathrm{df}' \quad \text{(A8)}$$

with Σ^{-1} defined through the relation:

$$\int_0^\infty \Sigma^{-1}(f,f')\Sigma(f',f'')\mathrm{df}' = \delta(\mathrm{f}-\mathrm{f}'')\,, \quad \text{(A9)}$$

where if we set in Eq.A9 that $\Sigma(f',f'') = \delta(f'-f'')S_n(f')$ we obtain

$$\Sigma^{-1}(f,f'')S_n(f'') = \delta(f-f'') \quad \text{(A10)}$$

and the inner product becomes

$$\begin{aligned}(a(t)|b(t)) &= 4\Re\int_0^\infty\int_0^\infty \frac{\tilde{a}^*(f)\,\delta(f-f')\tilde{b}(f')}{S_n(f')}\,\mathrm{df}\,\mathrm{df}' \\ &= 4\Re\int_0^\infty \frac{\tilde{a}^*(f)\tilde{b}(f)}{S_n(f)}\,\mathrm{df}\end{aligned} \quad \text{(A11)}$$

Appendix B: Fisher matrix derivation

1. Single detector

To compute the Fisher matrix of Eq. 8 we need the first derivative of the log-likelihood l with respect to the parameters of the power spectral density.

Here we present the derivation of the Fisher matrix for the noise parameters $\vec{\lambda}$ affecting the one-sided spectral density $S_n(f|\vec{\lambda})$, but this can be easily extended also including the gravitational wave background parameters $S_n(f|\vec{\lambda}) \to S_n(f|\vec{\lambda}) + S_{\rm GW}(f|\vec{\theta})$. We differentiate the log-likelihood of equation A6 with respect the parameters $\vec{\lambda}$:

$$\frac{\partial l}{\partial\lambda^i} = \sum_{k=1}^{n}[-\frac{1}{S_n(f_k)}\frac{\partial S_n(f_k)}{\partial\lambda^i} + \frac{1}{2}\frac{|\tilde{n}(f_k)|^2}{\frac{T}{4}S_n(f_k)^2}\frac{\partial S_n(f_k)}{\partial\lambda^i}], \quad \text{(B1)}$$

where we have omitted the dependency from $\vec{\lambda}$ to have a lighter notation. The second derivative of the likelihood is then

$$\begin{aligned}\frac{\partial^2 l}{\partial\lambda^i\partial\lambda^j} = \sum_{k=1}^{n}[&\frac{1}{S_n^2(f_k)}\frac{\partial S_n(f_k)}{\partial\lambda^i}\frac{\partial S_n(f_k)}{\partial\lambda^j} \\ &- \frac{1}{S_n(f_k)}\frac{\partial^2 S_n(f_k)}{\partial\lambda^i\partial\lambda^j} \\ &- \frac{1}{2}\frac{2|\tilde{n}(f_k)|^2}{\frac{T}{4}S_n(f_k)^3}\frac{\partial S_n(f_k)}{\partial\lambda^j}\frac{\partial S_n(f_k)}{\partial\lambda^i} \\ &+ \frac{1}{2}\frac{|\tilde{n}(f_k)|^2}{\frac{T}{4}S_n(f_k)^2}\frac{\partial^2 S_n(f_k)}{\partial\lambda^j\partial\lambda^i}]\end{aligned} \quad \text{(B2)}$$

using the definition of eq. (A4) the second and last term cancels and we get:

$$\Gamma_{ij} = \sum_{k=1}^{n} \frac{1}{S_n(f_k)^2} \frac{\partial S_n(f_k)}{\partial \lambda^i} \frac{\partial S_n(f_k)}{\partial \lambda^j} \,. \tag{B3}$$

If we want to get the continuum limit we need to recast a factor of Tdf:

$$\Gamma_{ij} = T \int_0^\infty \frac{1}{S_n(f)^2} \frac{\partial S_n(f)}{\partial \lambda^i} \frac{\partial S_n(f)}{\partial \lambda^j} \mathrm{df} \tag{B4}$$

2. Multiple detectors: real and imaginary part as separate random variables

If we want to generalize our derivation to multiple detectors or channels we need to define the noise properties of each channel. For simplicity let us consider two channels A and E with 4 independent random variables $X(f_k) = X_k = \{\Re[\tilde{X}^A_k], \Im[\tilde{X}^A_k], \Re[\tilde{X}^E_k], \Im[\tilde{X}^E_k]\}$ at each frequency f_k. Since the final likelihood will be given by the product over all the frequencies, we consider only one frequency and we drop the subscript "$_k$". We can specify the spectral densities of each channel and the cross-spectral densities with:

$$< \tilde{X}^{c*}(f')\tilde{X}^{c}(f) > = \frac{1}{2} S_c(f)\delta(f-f') \tag{B5a}$$

$$< \tilde{X}^{c}(f')\tilde{X}^{c}(f) > = 0 \tag{B5b}$$

$$< \tilde{X}^{E*}(f')\tilde{X}^{A}(f) > = \frac{1}{2} S^*_{AE}(f)\delta(f-f') \tag{B5c}$$

$$< \tilde{X}^{A*}(f')\tilde{X}^{E}(f) > = \frac{1}{2} S_{AE}(f)\delta(f-f') \tag{B5d}$$

$$< \tilde{X}^{A}(f')\tilde{X}^{E}(f) > = 0 \tag{B5e}$$

where the first two rows are valid for both channels $c = A, E$, and S_c is real and S_{AE} is complex. From the above expression we can deduce:

$$< \Re[\tilde{X}_c]\Re[\tilde{X}_c] > + < \Im[\tilde{X}_c]\Im[\tilde{X}_c] > = \frac{S_c}{2} \tag{B6a}$$

$$< \Re[\tilde{X}_c]\Re[\tilde{X}_c] - \Im[\tilde{X}_c]\Im[\tilde{X}_c] > = 0 \tag{B6b}$$

$$< \Re[\tilde{X}_c]\Im[\tilde{X}_c] > = 0 \tag{B6c}$$

$$< \Re[\tilde{X}_A]\Re[\tilde{X}_E] > + < \Im[\tilde{X}_A]\Im[\tilde{X}_E] > = \frac{\Re[S_{AE}]}{2} \tag{B6d}$$

$$< \Re[\tilde{X}_A]\Re[\tilde{X}_E] > - < \Im[\tilde{X}_A]\Im[\tilde{X}_E] > = 0 \tag{B6e}$$

$$< \Re[\tilde{X}_A]\Im[\tilde{X}_E] > - < \Im[\tilde{X}_A]\Re[\tilde{X}_E] > = \frac{\Im[S_{AE}]}{2} \tag{B6f}$$

$$< \Re[\tilde{X}_A]\Im[\tilde{X}_E] > + < \Im[\tilde{X}_A]\Re[\tilde{X}_E] > = 0\,, \tag{B6g}$$

where in the last four rows $c = A, E$. Note that these are in total 10 independent conditions (3 equations for A, 3 equations for E and 4 equations for AE) that specify uniquely the 10 independent elements of a symmetric covariance matrix.

For a single frequency we can generalize the likelihood to two channels as:

$$p(X) = \frac{1}{\sqrt{(2\pi)^{2\times N_c}\det(\Sigma)}} e^{-\frac{1}{2}X^T\Sigma^{-1}X} \tag{B7}$$

where $N_c = 2$ are the number of channels, X is a quadri-dimensional vector define above, Σ is the multiple-channels covariance matrix:

$$\Sigma = \begin{pmatrix} \frac{S_A}{4} & 0 & \frac{\Re(S_{AE})}{4} & \frac{\Im(S_{AE})}{4} \\ 0 & \frac{S_A}{4} & \frac{\Im(S_{AE})}{4} & \frac{\Re(S_{AE})}{4} \\ \frac{\Re(S_{AE})}{4} & \frac{\Im(S_{AE})}{4} & \frac{S_E}{4} & 0 \\ \frac{\Im(S_{AE})}{4} & \frac{\Im(S_{AE})}{4} & 0 & \frac{S_E}{4} \end{pmatrix} \tag{B8}$$

where here each element is evaluated at the fixed frequency. It can be shown that the expectation value of $X^T\Sigma^{-1}X$ equals the degrees of freedom, in this case 4. We have two channels, where each one has two degrees of freedom associated with the real and imaginary part of $\tilde{X}$.

We can then derive the Fisher matrix for the multiple channel case. Taking the first derivative of the log-likelihood

$$\frac{\partial \ln p(X)}{\partial \lambda^i} = -\frac{1}{2}\frac{1}{\det(\Sigma)}\frac{\partial \det(\Sigma)}{\partial \lambda^i} - \frac{1}{2}X^T\frac{\partial \Sigma^{-1}}{\partial \lambda^i}X \tag{B9}$$

where we can use the following property of the determinant:

$$\begin{aligned}\frac{\partial \det(\Sigma)}{\partial \lambda^i} &= \det(\Sigma)\ \mathrm{Tr}[\Sigma^{-1}\frac{\partial \Sigma}{\partial \lambda^i}] \\ &= \det(\Sigma)\ \left[\Sigma^{-1}\right]_{lm}\left[\frac{\partial \Sigma}{\partial \lambda^i}\right]^{ml}\end{aligned} \tag{B10}$$

to obtain

$$\frac{\partial \ln p(X)}{\partial \lambda^i} = -\frac{1}{2}\left[\Sigma^{-1}\right]_{lm}\left[\frac{\partial \Sigma}{\partial \lambda^i}\right]^{ml} - \frac{1}{2}X^T\frac{\partial \Sigma^{-1}}{\partial \lambda^i}X\,. \tag{B11}$$

Then, the second derivative of the log-likelihood takes the form:

$$\begin{aligned}\frac{\partial^2 \ln p(X)}{\partial \lambda^i \partial \lambda^j} &= -\frac{1}{2}\frac{\partial (\Sigma^{-1})^{lm}}{\partial \lambda^i}\frac{\partial \Sigma_{ml}}{\partial \lambda^j} \\ &\quad - \frac{1}{2}\Sigma^{-1}_{lm}\frac{\partial^2 \Sigma^{ml}}{\partial \lambda^i \partial \lambda^j} - \frac{1}{2}X^T\frac{\partial^2 \Sigma^{-1}}{\partial \lambda^i \lambda^j}X\end{aligned} \tag{B12}$$

.

We can finally compute the Fisher matrix for a single frequency with:

$$\Gamma_{ij} = \frac{1}{2}\Big[\frac{\partial \Sigma^{-1}_{lm}}{\partial \lambda^i}\frac{\partial \Sigma^{ml}}{\partial \lambda^j} + \Sigma^{-1}_{lm}\frac{\partial^2 \Sigma^{ml}}{\partial \lambda^i \partial \lambda^j} + \Sigma_{ml}\frac{\partial^2 (\Sigma^{-1})^{lm}}{\partial \lambda^i \lambda^j}\Big], \tag{B13}$$

where we have considered $< X^T_l \frac{\partial^2 \Sigma^{-1}_{lm}}{\partial \lambda^i \lambda^j} X_m >= \frac{\partial^2 \Sigma^{-1}_{lm}}{\partial \lambda^i \lambda^j}\Sigma_{ml}$. If we use the property

$$\frac{\partial (\Sigma)^{-1}_{lm}}{\partial \lambda} = -(\Sigma)^{-1}_{ln}\frac{\partial (\Sigma)_{nq}}{\partial \lambda}(\Sigma)^{-1}_{qm} \tag{B14}$$

we obtain the following expression:

$$\Gamma_{ij} = \frac{1}{2}\mathrm{Tr}\Big[-\Sigma^{-1}\frac{\partial\Sigma}{\partial\lambda^{\mathrm{i}}}\Sigma^{-1}\frac{\partial\Sigma}{\partial\lambda^{\mathrm{j}}} + \Sigma^{-1}\frac{\partial^2\Sigma}{\partial\lambda^{\mathrm{i}}\partial\lambda^{\mathrm{j}}} + \Sigma\frac{\partial^2\Sigma^{-1}}{\partial\lambda^{\mathrm{i}}\partial\lambda^{\mathrm{j}}}\Big] \tag{B15}$$

which can be further simplified if we use the following properties:

$$\partial(\Sigma\Sigma^{-1}) = 0 \tag{B16a}$$
$$\partial\Sigma\Sigma^{-1} + \Sigma\partial\Sigma^{-1} = 0 \tag{B16b}$$
$$\partial^2\Sigma\Sigma^{-1} + 2\partial\Sigma\partial\Sigma^{-1} + \Sigma\partial^2\Sigma^{-1} = 0 \tag{B16c}$$
$$\partial^2\Sigma\Sigma^{-1} - 2\partial\Sigma\,\Sigma^{-1}\,\partial\Sigma\,\Sigma^{-1} + \Sigma\partial^2\Sigma^{-1} = 0 \tag{B16d}$$

Note that in the above expression the first and last term of Eq.B16d correspond to the last two terms in the Fisher matrix expression (B15). The final expression for all frequencies can be easily obtained by taking the sum over all the frequencies:

$$\Gamma_{ij} = \frac{1}{2}\sum_{k=1}^{n}[(\Sigma_k^{-1})_{lr}\frac{\partial\Sigma_k^{rp}}{\partial\lambda^i}(\Sigma_k^{-1})_{pm}\frac{\partial\Sigma_k^{ml}}{\partial\lambda^j}]\,. \tag{B17}$$

Note that there is an additional factor of $1/2$ with respect to Eq. B3. If we insert only the first 2 columns and rows of Σ we obtain the previous equation for the single channel as expected.

3. Multiple detectors: complex random variables

Equivalently, the likelihood can be written in terms of complex variables $\tilde{X}_A$ and $\tilde{X}_E$ [38]

$$p(\tilde{X}_A, \tilde{X}_E) = \frac{e^{-[\tilde{X}_A,\tilde{X}_E]^{\mathrm{H}}\Sigma^{-1}[\tilde{X}_A,\tilde{X}_E]}}{(2\pi)^{N_c}\det(\Sigma_k)} \tag{B18}$$

where "H" indicates the Hermitian conjugate, the factor of $1/2$ disappeared because it is a complex distribution and must match Eqs (B7)–(B8), and the new complex covariance matrix is defined as

$$\Sigma = \frac{1}{2}\begin{pmatrix} S_A & S_{AE} \\ S_{AE}^* & S_E \end{pmatrix}\,, \tag{B19}$$

where Σ is now an Hermitian matrix and can be obtained from the conditions imposed in Eqs. B5. The expectation value of $[\tilde{X}_A, \tilde{X}_E]^{\mathrm{H}}\Sigma^{-1}[\tilde{X}_A, \tilde{X}_E]$ over complex variable realizations $[\tilde{X}_A, \tilde{X}_E]$ is now 2. However, since the exponential does not have any factor of $1/2$ for a complex distribution, we recover the same number of degrees of freedom in the argument of the exponent as in the previous derivation, i.e. we got $\exp[\frac{1}{2}4]$ for the case of multiple detectors with real and imaginary part as separate random variables' and $\exp[2]$ for the case considered here.

The derivation of the Fisher matrix differs from the previous one (Eq. B17) only by the factor $1/2$:

$$\Gamma_{ij} = \sum_{k=1}^{n}\left[(\Sigma_k^{-1})_{lr}\frac{\partial\Sigma_k^{rp}}{\partial\lambda^i}(\Sigma_k^{-1})_{pm}\frac{\partial\Sigma_k^{ml}}{\partial\lambda^j}\right], \tag{B20}$$

where the matrix Σ_k is given by Σ with spectral densities evaluated at given frequency f_k.
Note that we can recover the single channel realization by using the first element of Σ.
The continuum limit of the Fisher matrix in this formulation is given by

$$\Gamma_{ij} = T\int_0^\infty (\Sigma_k^{-1})_{lr}\frac{\partial\Sigma_k^{rp}}{\partial\lambda^i}(\Sigma_k^{-1})_{pm}\frac{\partial\Sigma_k^{ml}}{\partial\lambda^j}\,\mathrm{df}\,. \tag{B21}$$

4. Deterministic sources and noise cross-correlation

In the presence of a deterministic source, $\tilde{h}(f_k|\vec{\mu})$, the derivative of the log-likelihood in Eq. (7) with respect to the source parameters, $\vec{\mu}$, is:

$$\frac{\partial l}{\partial\mu^i} = -\sum_{k=1}^{n}\frac{|\tilde{s}(f_k) - \tilde{h}(f_k|\vec{\mu})|}{\frac{T}{4}S_n(f_k|\vec{\lambda})}\frac{\partial\tilde{h}(f_k|\vec{\mu})}{\partial\mu^i}\,, \tag{B22}$$

and the derivative with respect to the parameters characterising the spectral density, $\vec{\lambda}$, is:

$$\frac{\partial l}{\partial\lambda^i} = \sum_{k=1}^{n}[-\frac{1}{2}\frac{T}{\det(S_n(f_k|\vec{\lambda}))} + \\ + \frac{|\tilde{s}(f_k) - \tilde{h}(f_k|\vec{\mu})|^2}{\frac{T}{2}S_n(f_k|\vec{\lambda})^2}]\frac{\partial S_n(f_k|\vec{\lambda})}{\partial\lambda^i}\,. \tag{B23}$$

The first of these expressions is odd in the noise component, $\tilde{n}(f_k) = \tilde{s}(f_k) - \tilde{h}(f_k|\vec{\mu})$, while the second term is even. Since $\mathbb{E}[\tilde{n}(f_k)] = 0$, from this we deduce that

$$\mathbb{E}_{\mathcal{L}}\left[\frac{\partial l}{\partial\mu^i}\frac{\partial l}{\partial\lambda^j}\right] = 0, \tag{B24}$$

i.e., at this level of approximation the terms in the Fisher matrix that mix signal and noise parameters vanish. We conclude that the estimation of the noise parameters and of the signal parameters is, at leading order, independent. Lack of knowledge of the noise should therefore not significantly affect measurements of the parameters of deterministic signals, except indirectly through the change in the spectral density that enters the likelihood for the deterministic sources.

Appendix C: Impact of instrumental noise knowledge uncertainty on SGWB recovery in absence of galactic foreground

Below we show the same computations we did in Sec. III but in case we do not consider the presence of the foreground.

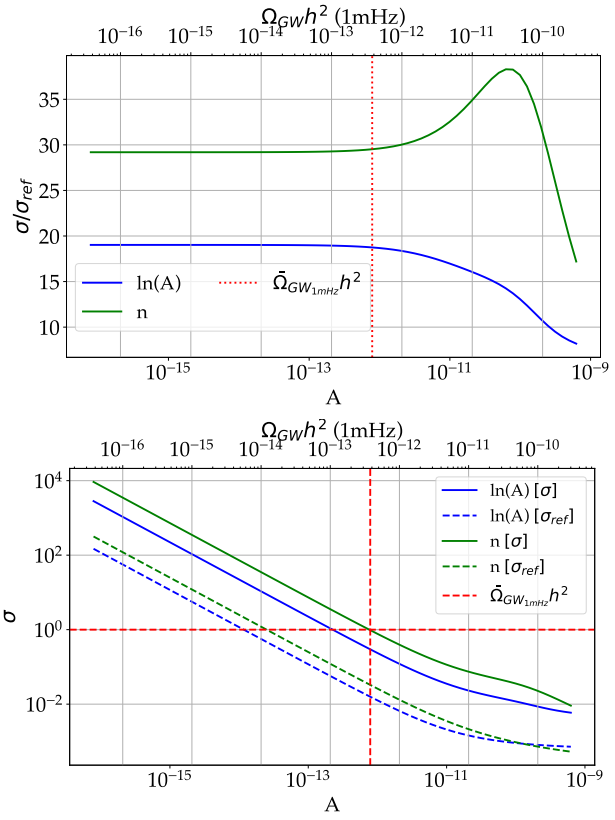

FIG. 18. Results for the power law SGWB model without foreground

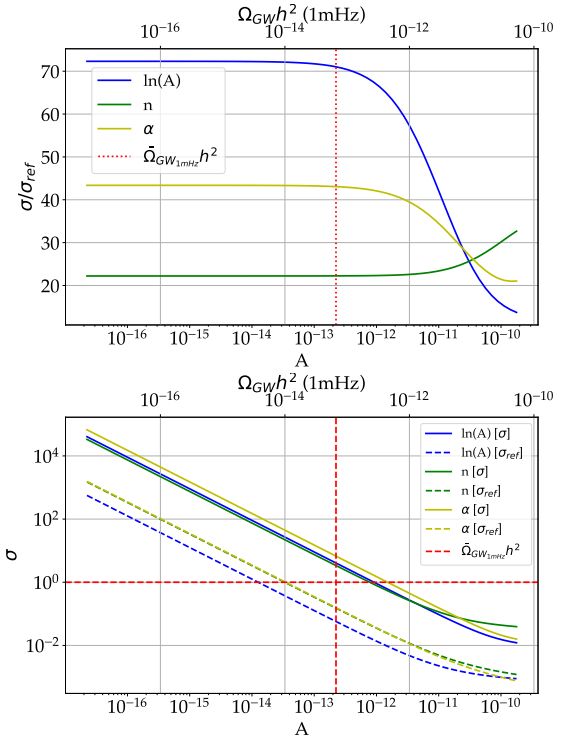

FIG. 19. Results for the power-law with running SGWB model without foreground.

a. *Power law*

Figure 18 shows the results computed for the power law model. We see that in the presence of instrumental noise uncertainties, the uncertainty in the SGWB parameters increases by a factor of $\sim$ 19–36, with the uncertainty in the slope being more affected than that of the amplitude. Considering the raw uncertainties, to achieve the same measurement precision, the background energy density would have to be $\sim$ 33 times larger than it would need to be in the absence of noise knowledge uncertainties. However, a background with amplitude equal to the reference value should be detectable even allowing for confusion with instrumental noise mis-modelling.

b. *Power law with running*

The results for this model are shown in Figure 19. In this case we see that the uncertainties in the SGWB parameters increase by a factor of $\sim$ 21–72, with the uncertainty on the log-amplitude being most affected in this case. Once again, the relative increase in the uncertainty is somewhat lower at higher background amplitudes. The lower panel of fig. 19 shows that the background is not detectable at the reference amplitude. An energy density $\sim$ 5 times higher would be required for a detection. In general, the background again has to have an energy density $\sim$ 100 times higher to be characterised with the same measurement precision when there is instrumental noise uncertainty as it could be without those uncertainties.

c. *Gaussian bump*

The results for this model are shown in Figure 20. In this case, the degradation in the precision of parameter measurement is a factor of $\sim$ 2.3–4 when allowing for lack of knowledge of the instrumental noise. From the lower panel of Figure 20 we see that the energy density in a Gaussian bump SGWB has to be just a small factor of $\sim$ 2.5 times bigger to achieve the same measurement precision when the instrumental noise is not known perfectly. Moreover a Gaussian bump background at the reference amplitude can be measured to percent precision at the reference amplitude. The width of the Gaussian can be measured to a few tens of percent precision at the reference amplitude, improving approximately linearly with the background energy density.

d. *First order phase transition*

The results for First order phase transition are shown in Figure 21. The results for this SGWB model are quite

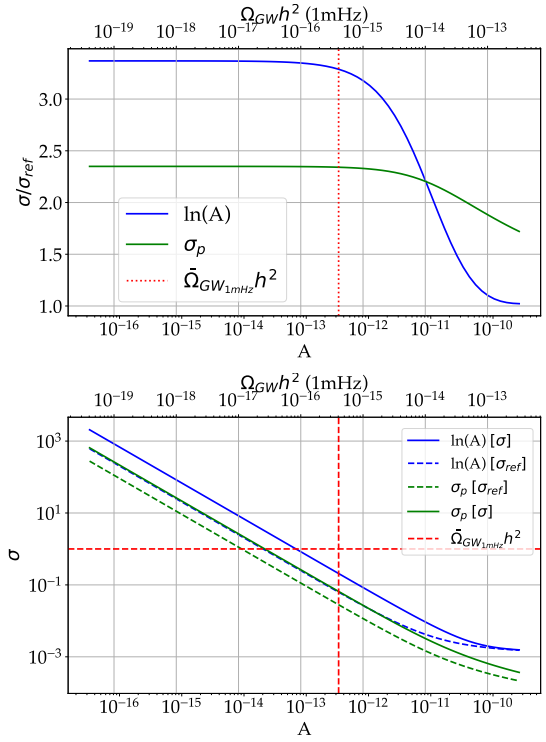

FIG. 20. Results for Gaussian bump SGWB model without foreground

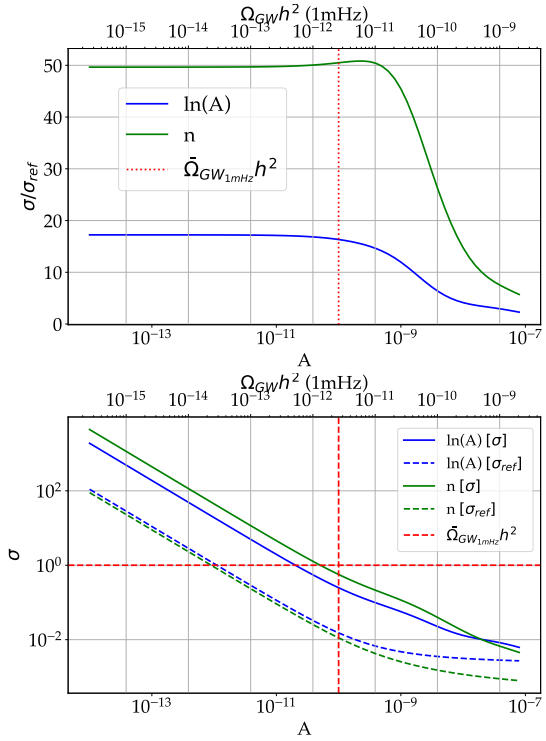

FIG. 21. Results for first order phase transition SGWB model without foreground.

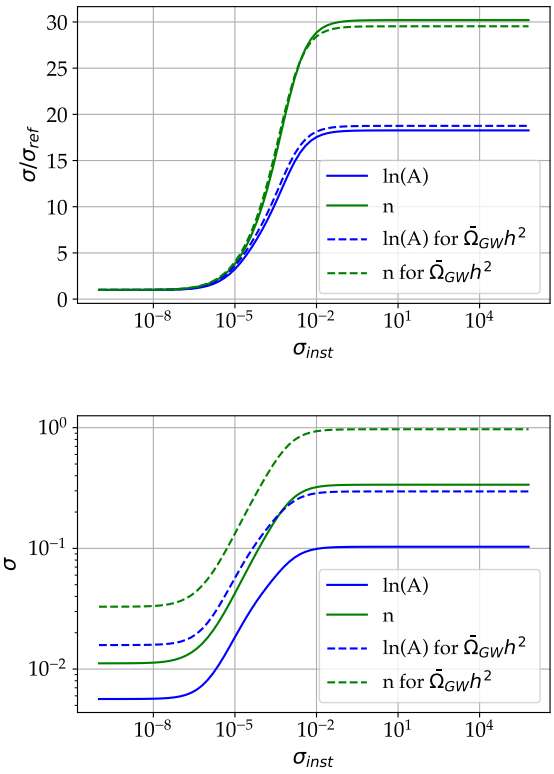

FIG. 22. As Figure 18, but now for fixed background amplitude and varying the variance of the Gaussian prior on the instrumental noise spline model. This plot is for a power law background, and the amplitude has been fixed such that the SNR in TDI channel A is 136 (continous lines) and 43 (dashed lines)

similar to those for the power law background. When allowing for instrumental noise knowledge uncertainties, the precision with which the SGWB log-amplitude can be characterised degrades by a factor of $\sim$ 18. The degradation in the determination of the spectral index is even larger, $\sim$ 50. Once again, to achieve the same measurement precision, the background energy density would have to be $\sim$ 50 times larger than it would need to be in the absence of noise knowledge uncertainties. Nonetheless, a FOPT background at the reference amplitude would still be detectable and provide a measurement of the spectral index at the level of about 0.5 percent.

We can do the same analysis we did in section III B but without including the foreground. The results for all four SGWB models are qualitatively similar among themselves and also to the previous case with foreground in Sec. III B. Figure 22 consider the power law case, Fig. 23 the case of power law with running, Fig. 24 the case of gaussian model and Fig. 25 the case of FOPT model.

The main conclusion from these results is that again if we wanted to ensure that there was no degradation

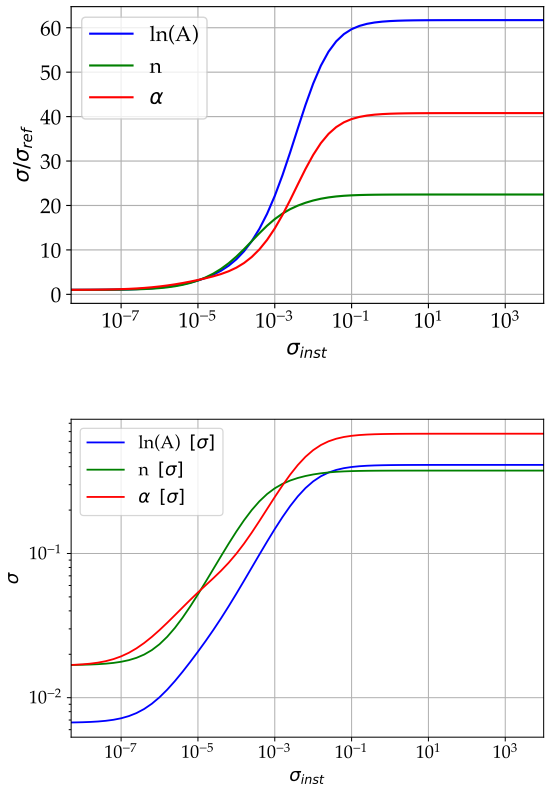

FIG. 23. As Figure 22 but now for the power-law-with-running model. The background amplitude has been fixed to give an overall SNR of 145.

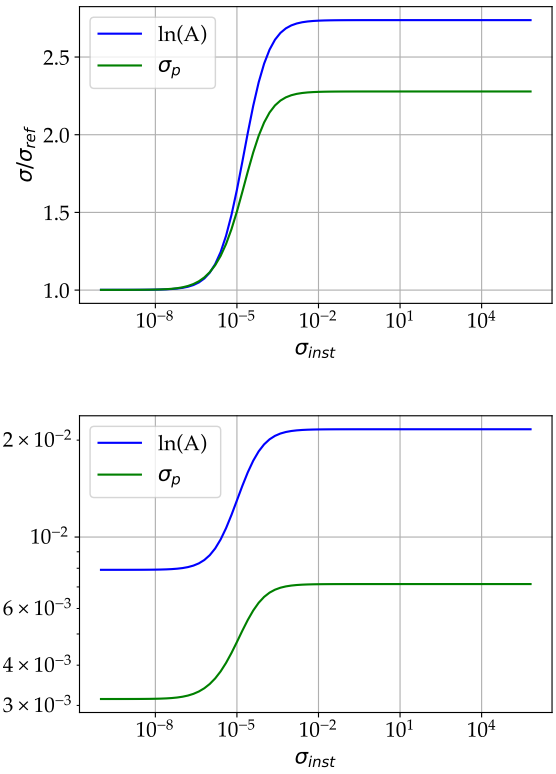

FIG. 24. As Figure 22 but now for the Gaussian bump model. The background amplitude has been fixed to give an overall SNR of 135.

in LISA science due to lack of noise knowledge, the necessary requirement on the noise knowledge would be $\ll 10\%$.

1. Signal reconstruction without foreground of Galactic binaries

We consider a power law signal with an SNR of 48.70 in Fig. 26. The three panels show the reconstructed ASDs for the SGWB and for the instrumental noise and the total, which is the sum of the three. No foreground has been considered in this case. In Fig 27 we show corresponding results for a power law with a higher SNR, of 862.

We see that our ability to reconstruct the signal component of the data stream is poor when the SNR is low. However, we are able to obtain good measurements of the instrumental noise and the total spectral density. We note that the total ASD reconstruction in Figure 26 is somewhat poorer than the noise-only component, which does not fit with the expectation that we are actually measuring the total. This happens due to the breakdown in the Fisher matrix approximation for the SGWB parameters in this case, because the SGWB parameter uncertainties are large and no longer in the linear signal regime. At higher SNR, we start to be able to reconstruct the SGWB more precisely, shown by a reduction in the scatter in Figure 27. As the SNR is increased we would expect the scatter to reduce further. The reconstruction of the noise spectral density is comparable to what is seen in the lower SNR case, but we would eventually expect it to degrade as the SGWB becomes more dominant in the data. The reconstruction of the total spectral density is similar to the low SNR case, as expected. However, this higher SNR case does not show the noise at low frequency that arises from the breakdown of the Fisher matrix approximation, presumably because the measurement uncertainties are within the linear regime in this case. although, what is interesting to notice in the total reconstruction is that the channels A and E are affected by the SGWB where between $1mHz$ and $4mHz$ the noise level deviated from the expected one shown in Fig 2.

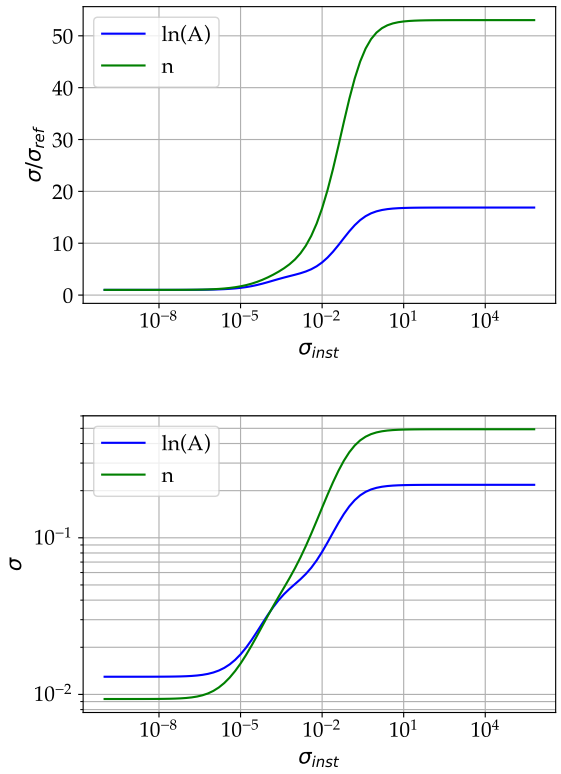

FIG. 25. As Figure fig. 22 but now for the FOPT model. The background amplitude has been fixed to give an overall SNR of 149.

[1] Lisa red-book, in prep.

[2] Matthew R. Adams and Neil J. Cornish. Discriminating between a Stochastic Gravitational Wave Background and Instrument Noise. Phys. Rev. D, 82:022002, 2010.

[3] Bruce Allen and Joseph D. Romano. Detecting a stochastic background of gravitational radiation: Signal processing strategies and sensitivities. Phys. Rev. D, 59(10):102001, May 1999.

[4] Pau Amaro-Seoane et al. Laser Interferometer Space Antenna. 2 2017.

[5] M. Armano, H. Audley, G. Auger, J. T. Baird, M. Bassan, P. Binetruy, M. Born, D. Bortoluzzi, N. Brandt, M. Caleno, L. Carbone, A. Cavalleri, A. Cesarini, G. Ciani, G. Congedo, A. M. Cruise, K. Danzmann, M. de Deus Silva, R. De Rosa, M. Diaz-Aguiló, L. Di Fiore, I. Diepholz, G. Dixon, R. Dolesi, N. Dunbar, L. Ferraioli, V. Ferroni, W. Fichter, E. D. Fitzsimons, R. Flatscher, M. Freschi, A. F. García Marín, C. García Marirrodriga, R. Gerndt, L. Gesa, F. Gibert, D. Giardini, R. Giusteri, F. Guzmán, A. Grado, C. Grimani, A. Grynagier, J. Grzymisch, I. Harrison, G. Heinzel, M. Hewitson, D. Hollington, D. Hoyland, M. Hueller, H. Inchauspé, O. Jennrich, P. Jetzer, U. Johann, B. Johlander, N. Karnesis, B. Kaune, N. Korsakova, C. J. Killow, J. A. Lobo, I. Lloro, L. Liu, J. P. López-Zaragoza, R. Maarschalkerweerd, D. Mance, V. Martín, L. Martin-Polo, J. Martino, F. Martin-Porqueras, S. Madden, I. Mateos, P. W. McNamara, J. Mendes, L. Mendes, A. Monsky, D. Nicolodi, M. Nofrarias, S. Paczkowski, M. Perreur-Lloyd, A. Petiteau, P. Pivato, E. Plagnol, P. Prat, U. Ragnit, B. Raïs, J. Ramos-Castro, J. Reiche, D. I. Robertson, H. Rozemeijer, F. Rivas, G. Russano, J. Sanjuán, P. Sarra, A. Schleicher, D. Shaul, J. Slutsky, C. F. Sopuerta, R. Stanga, F. Steier, T. Sumner, D. Texier, J. I. Thorpe, C. Trenkel, M. Tröbs, H. B. Tu, D. Vetrugno, S. Vitale, V. Wand, G. Wanner, H. Ward, C. Warren, P. J. Wass, D. Wealthy, W. J. Weber, L. Wissel, A. Wittchen, A. Zambotti, C. Zanoni, T. Ziegler, and P. Zweifel. Sub-femto-g free fall for space-based gravitational wave observatories: Lisa pathfinder results. Phys. Rev. Lett., 116:231101, Jun 2016.

[6] J. W. Armstrong, F. B. Estabrook, and Massimo Tinto. Time-delay interferometry for space-based gravitational wave searches. The Astrophysical Journal, 527(2):814, dec 1999.

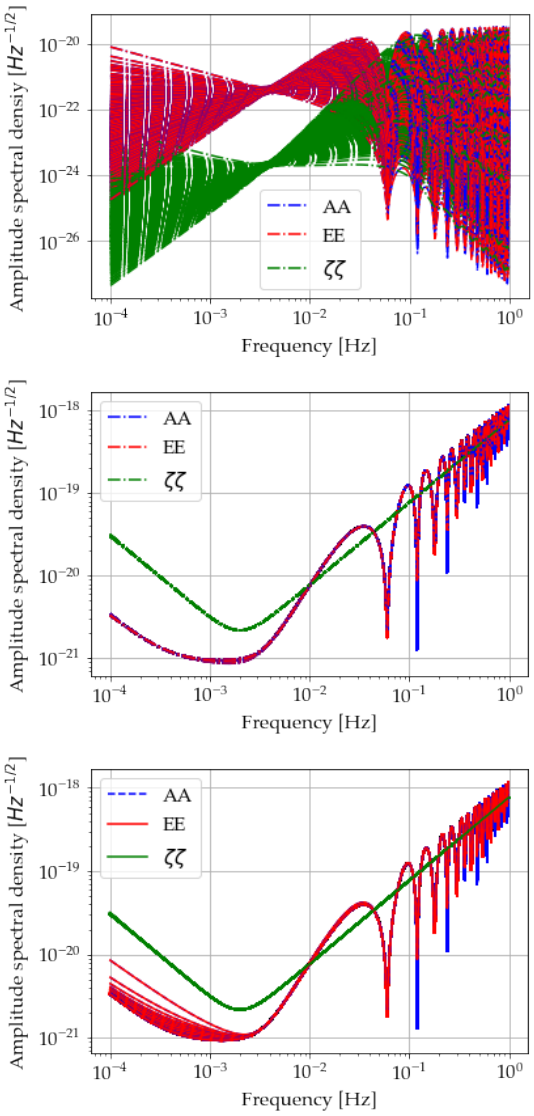

FIG. 26. Signal and noise reconstruction for a power law SGWB with SNR 48.70. We show the signal and noise PSDs corresponding to random draws from the posterior, approximated using the Fisher matrix as described in the text. In each panel the curves correspond to the three TDI channels: A (blue), E (red) and ζ (green). Upper panel: reconstructed SGWB; middle panel: reconstructed instrumental noise; lower panel: total reconstructed ASD (signal + noise).

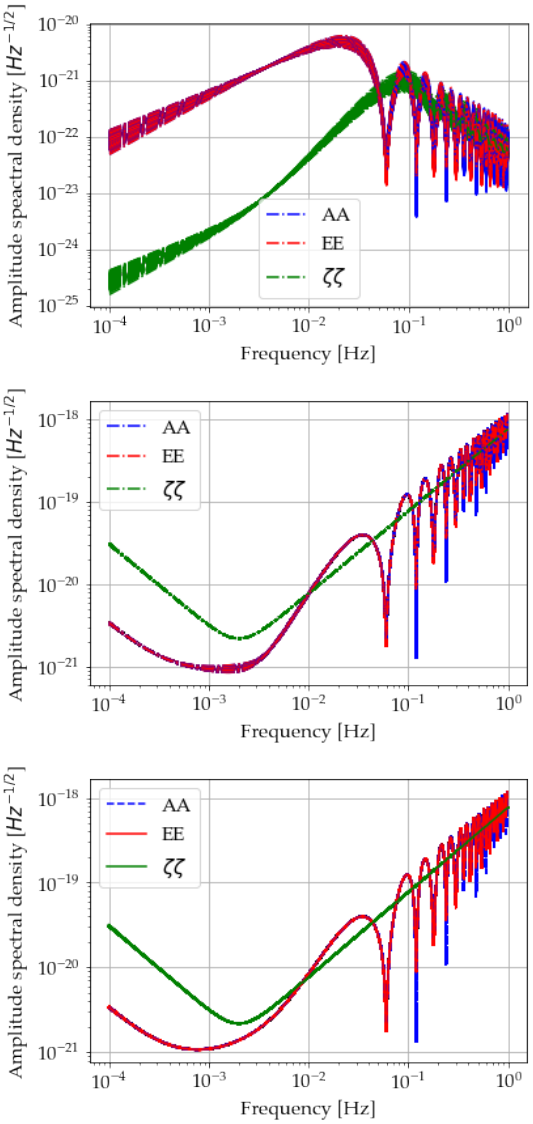

FIG. 27. As Figure 26, but for a power law background with higher SNR, of 862.

[7] Stanislav Babak, Chiara Caprini, Daniel G. Figueroa, Nikolaos Karnesis, Paolo Marcoccia, Germano Nardini, Mauro Pieroni, Angelo Ricciardone, Alberto Sesana, and Jesús Torrado. Stochastic gravitational wave background from stellar origin binary black holes in lisa, 2023.

[8] Stanislav Babak, Jonathan Gair, Alberto Sesana, Enrico Barausse, Carlos F. Sopuerta, Christopher P. L. Berry, Emanuele Berti, Pau Amaro-Seoane, Antoine Petiteau, and Antoine Klein. Science with the space-based interferometer LISA. V: Extreme mass-ratio inspirals. Phys. Rev. D, 95(10):103012, 2017.

[9] Stanislav Babak, Antoine Petiteau, and Martin Hewitson. LISA Sensitivity and SNR Calculations. 8 2021.

[10] Quentin Baghi, Nikolaos Karnesis, Jean-Baptiste Bayle, Marc Besançon, and Henri Inchauspé. Uncovering gravitational-wave backgrounds from noises of unknown shape with LISA. 2 2023.

[11] N. Bartolo, V. De Luca, G. Franciolini, A. Lewis, M. Peloso, and A. Riotto. Primordial Black Hole Dark Matter: LISA Serendipity. Phys. Rev. Lett., 122(21):211301, 2019.

[12] N. Bartolo, V. De Luca, G. Franciolini, M. Peloso, D. Racco, and A. Riotto. Testing primordial black holes as dark matter with LISA. Physical Review D, 99(10), may 2019.

[13] Nicola Bartolo et al. Science with the space-based interferometer LISA. IV: Probing inflation with gravitational waves. JCAP, 12:026, 2016.

[14] Jean-Baptiste Bayle, Aurélien Hees, Marc Lilley, and Christophe Le Poncin-Lafitte. Lisa orbits, April 2022.

[15] Chiara Caprini and Daniel G. Figueroa. Cosmological Backgrounds of Gravitational Waves. Class. Quant. Grav., 35(16):163001, 2018.

[16] Chiara Caprini, Daniel G. Figueroa, Raphael Flauger, Germano Nardini, Marco Peloso, Mauro Pieroni, Angelo Ricciardone, and Gianmassimo Tasinato. Reconstructing the spectral shape of a stochastic gravitational wave background with LISA. Journal of Cosmology and Astroparticle Physics, 2019(11):017–017, nov 2019.

[17] Chiara Caprini, Mark Hindmarsh, Stephan Huber, Thomas Konstandin, Jonathan Kozaczuk, Germano Nardini, Jose Miguel No, Antoine Petiteau, Pedro Schwaller, Gé raldine Servant, and David J. Weir. Science with the space-based interferometer eLISA. II: gravitational waves from cosmological phase transitions. Journal of Cosmology and Astroparticle Physics, 2016(04):001–001, apr 2016.

[18] M. Chwalla, K. Danzmann, M. Dovale Álvarez, J.J. Esteban Delgado, G. Fernández Barranco, E. Fitzsimons, O. Gerberding, G. Heinzel, C.J. Killow, M. Lieser, M. Perreur-Lloyd, D.I. Robertson, J.M. Rohr, S. Schuster, T.S. Schwarze, M. Tröbs, G. Wanner, and H. Ward. Optical suppression of tilt-to-length coupling in the lisa long-arm interferometer. Phys. Rev. Appl., 14:014030, Jul 2020.

[19] LISA Pathfinder collaboration. In-depth analysis of LISA Pathfinder performance results: time evolution, noise projection, physical models and implications for LISA.

[20] Raphael Flauger, Nikolaos Karnesis, Germano Nardini, Mauro Pieroni, Angelo Ricciardone, and Jesús Torrado. Improved reconstruction of a stochastic gravitational wave background with LISA. JCAP, 01:059, 2021.

[21] G. Franciolini. Primordial black holes: from theory to gravitational wave observations, 2021.

[22] Davide Gerosa, Sizheng Ma, Kaze W. K. Wong, Emanuele Berti, Richard O'Shaughnessy, Yanbei Chen, and Krzysztof Belczynski. Multiband gravitational-wave event rates and stellar physics. Phys. Rev. D, 99(10):103004, 2019.

[23] Marie-Sophie Hartig, Sönke Schuster, and Gudrun Wanner. Geometric tilt-to-length coupling in precision interferometry: mechanisms and analytical descriptions. Journal of Optics, 24(6):065601, may 2022.

[24] Olaf Hartwig. Instrumental modelling and noise reduction algorithms for the laser interferometer Gravitational-wave Observatory, PhD thesis, Leibniz U., Hannover, 2021.

[25] Olaf Hartwig and Jean-Baptiste Bayle. Clock-jitter reduction in lisa time-delay interferometry combinations. Phys. Rev. D, 103:123027, Jun 2021.

[26] Olaf Hartwig, Marc Lilley, Martina Muratore, and Mauro Pieroni. Stochastic gravitational wave background reconstruction for a non-equilateral and unequal-noise LISA constellation. 3 2023.

[27] Olaf Hartwig and Martina Muratore. Characterization of time delay interferometry combinations for the lisa instrument noise. Phys. Rev. D, 105:062006, Mar 2022.

[28] Mark Hindmarsh, Stephan J. Huber, Kari Rummukainen, and David J. Weir. Shape of the acoustic gravitational wave power spectrum from a first order phase transition. Phys. Rev. D, 96:103520, Nov 2017.

[29] Antoine Klein et al. Science with the space-based interferometer eLISA: Supermassive black hole binaries. Phys. Rev. D, 93(2):024003, 2016.

[30] Leonard Lehoucq, Irina Dvorkin, Rahul Srinivasan, Clement Pellouin, and Astrid Lamberts. Astrophysical uncertainties in the gravitational-wave background from stellar-mass compact binary mergers, 2023.

[31] Christopher J. Moore, Davide Gerosa, and Antoine Klein. Are stellar-mass black-hole binaries too quiet for LISA? Mon. Not. Roy. Astron. Soc., 488(1):L94–L98, 2019.

[32] Martina Muratore. Time delay interferometry for LISA science and i PhD thesis, Trento U., 2021.

[33] Martina Muratore, Olaf Hartwig, Daniele Vetrugno, Stefano Vitale, and William Joseph Weber. On the effectiveness of null TDI channels as instrument noise monitors in LISA. 7 2022.

[34] Martina Muratore, Daniele Vetrugno, and Stefano Vitale. Revisitation of time delay interferometry combinations that suppress laser noise in lisa, 2020.

[35] Martina Muratore, Daniele Vetrugno, Stefano Vitale, and Olaf Hartwig. Time delay interferometry combinations as instrument noise monitors for LISA. Phys. Rev. D, 105(2):023009, 2022.

[36] Dam Quang Nam, Yves Lemiere, Antoine Petiteau, Jean-Baptiste Bayle, Olaf Hartwig, Joseph Martino, and Martin Staab. Tdi noises transfer functions for lisa, 2022.

[37] S. Paczkowski, R. Giusteri, M. Hewitson, N. Karnesis, E. D. Fitzsimons, G. Wanner, and G. Heinzel. Postprocessing subtraction of tilt-to-length noise in lisa. Phys. Rev. D, 106:042005, Aug 2022.

[38] B. Picinbono. Second-order complex random vectors and normal distributions. IEEE Transactions on Signal Processing, 44(10):2637–2640, 1996.

[39] Thomas A. Prince, Massimo Tinto, Shane L. Larson, and J. W. Armstrong. Lisa optimal sensitivity. Phys. Rev. D, 66:122002, Dec 2002.

[40] Wen-Hong Ruan, Zong-Kuan Guo, Rong-Gen Cai, and Yuan-Zhong Zhang. Taiji Program: Gravitational-Wave Sources. arXiv e-prints, page arXiv:1807.09495, July 2018.

[41] Lorenzo Sala. Residual test mass acceleration in LISA Pathfinder: in PhD thesis, University of Trento, 2023.

[42] Eric Savalle, Jonathan Gair, Lorenzo Speri, and Stanislav Babak. Assessing the impact of instrumental calibration uncertainty on LISA science. Physical Review D, 106(2), jul 2022.

[43] Alberto Sesana. Prospects for multiband gravitational-wave astronomy after gw150914. Phys. Rev. Lett., 116:231102, Jun 2016.

[44] Eric Thrane and Joseph D. Romano. Sensitivity curves for searches for gravitational-wave backgrounds. Phys. Rev. D, 88(12):124032, 2013.

[45] M. Tinto and S.V Dhurandhar. Time-delay interferometry. Living Rev Relativ 24, 2021.

[46] Massimo Tinto and Olaf Hartwig. Time-Delay Interferometry and Clock-Noise Calibration. Phys. Rev. D, 98(4):042003, 2018.